

A Decade of SCUBA-2: A Comprehensive Guide to Calibrating 450 μm and 850 μm Continuum Data at the JCMT

STEVE MAIRS,¹ JESSICA T. DEMPSEY,¹ GRAHAM S. BELL,¹ HARRIET PARSONS,¹ MALCOLM J. CURRIE,^{1,2} PER FRIBERG,¹
XUE-JIAN JIANG,¹ ALEXANDRA J. TETARENKO,¹ DAN BINTLEY,¹ JAMIE COOKSON,¹ SHAOLIANG LI,¹ MARK G. RAWLINGS,¹
JAN WOUTERLOOT,¹ DAVID BERRY,¹ SARAH GRAVES,¹ IZUMI MIZUNO,¹ ALEXIS ANN ACOHIDO,¹ ALYSSA CLARK,¹
JEFF COX,³ MIRIAM FUCHS,¹ JAMES HOGE,¹ JOHNATHON KEMP,³ E'LISA LEE,¹ CALLIE MATULONIS,¹
WILLIAM MONTGOMERIE,^{1,4} KEVIN SILVA,¹ AND PATRICE SMITH¹

¹*East Asian Observatory, 660 N. A'ohōkū Place, Hilo, HI 96720, USA*

²*RAL Space, STFC Rutherford Appleton Laboratory, Chilton, Didcot, Oxfordshire OX11 0QX, UK*

³*Joint Astronomy Centre, 660 N. A'ohōkū Place, Hilo, HI 96720, USA*

⁴*SOFIA Science Center, Universities Space Research Association, NASA Ames Research Center, Moffett Field, CA 94035, USA*

(Accepted July 30, 2021)

Submitted to AJ

ABSTRACT

The Submillimetre Common User Bolometer Array 2 (SCUBA-2) is the James Clerk Maxwell Telescope's continuum imager, operating simultaneously at 450 and 850 μm . SCUBA-2 was commissioned in 2009–2011 and since that time, regular observations of point-like standard sources have been performed whenever the instrument is in use. Expanding the calibrator observation sample by an order of magnitude compared to previous work, in this paper we derive updated opacity relations at each wavelength for a new atmospheric-extinction correction, analyze the Flux-Conversion Factors (FCFs) used to convert instrumental units to physical flux units as a function of date and observation time, present information on the beam profiles for each wavelength, and update secondary-calibrator source fluxes. Between 07:00 and 17:00 UTC, the portion of the night that is most stable to temperature gradients that cause dish deformation, the total-flux uncertainty and the peak-flux uncertainty measured at 450 μm are found to be 14% and 17%, respectively. Measured at 850 μm , the total-flux and peak-flux uncertainties are 6%, and 7%, respectively. The analysis presented in this work is applicable to all SCUBA-2 projects observed since 2011.

Keywords: techniques: image processing – methods: data analysis – techniques: photometric

1. INTRODUCTION

Ground-based submillimeter observations are subject to severe attenuation of the incoming light due to absorption by atmospheric water vapor. There are few sites on Earth that are dry enough to allow for significant transmission of submillimeter light in a series of narrow wavebands; Maunakea, The Atacama Desert, and Antarctica are among them. The Submillimetre Common User Bolometer Array 2 (SCUBA-2; see [Holland et al. 2013](#) for details), installed at the 15 m James Clerk Maxwell Telescope (JCMT) in 2009 capitalises on

two such wavebands centred on 450 and 850 μm . Situated at an altitude of 4,092 meters near the summit of Maunakea, this continuum imager consists of two focal planes, each comprising 5,120 Transition Edge Sensors (TES) allowing data to be obtained at both wavelengths simultaneously. The half-power bandwidths of the band-pass filters are 32 and 85 μm at 450 and 850 μm , respectively.

SCUBA-2 maps the sky more than 100 times faster than its predecessor, SCUBA ([Holland et al. 1999](#)), which was decommissioned in 2005. Since its installation at the JCMT, SCUBA-2 has proven to be a workhorse instrument, providing invaluable data on a variety of fields including studies focused on the thermal dust emission associated with the earliest stages of

star formation (e.g. Ward-Thompson et al. 2007; Hercezeg et al. 2017; Liu et al. 2018), the mass-loss history of evolved stars (e.g. Dharmawardena et al. 2019), the properties of active comets (e.g. Coulson et al. 2020), the evolution of nearby galaxies (e.g. Wilson et al. 2009; Saintonge et al. 2018; Li et al. 2020), number counts of distant, submillimeter galaxies (e.g. Geach et al. 2013; Wang et al. 2017; Simpson et al. 2019; Shim et al. 2020), black holes (e.g. Tetarenko et al. 2017), and transient phenomena (e.g. Mairs et al. 2018; Smith et al. 2018; Mairs et al. 2019). SCUBA-2 is also the detector used in conjunction with the JCMT’s linear polarimeter, POL-2 (Friberg et al. 2018) to obtain Stokes I , Q , and U parameters, providing information on interstellar magnetic fields (e.g. Ward-Thompson et al. 2017).

Despite the unprecedented collecting power and sensitivity of SCUBA-2, the atmospheric opacity still poses an issue for calibration as it is variable over short timescales and highly dependent on the amount of precipitable water vapor (PWV) present along the line of sight. In order to robustly calibrate the data, this loss of light must be well modeled and empirically understood. To this end, high-cadence measurements of the PWV are obtained along the line of sight during SCUBA-2 observations (Dempsey & Friberg 2008) in order to calculate and correct for the expected atmospheric extinction in the images (Chapin et al. 2013).

In addition to the variable atmosphere, changes in the optical path of the instrument such as thermal-filter changes, secondary-mirror adjustments, or the removal of the JCMT’s GORE-TEX™ membrane can also affect the final data. SCUBA-2 commissioning took place between 2009 October and 2011 September. Instrument performance and commissioning details throughout this time are presented in Bintley et al. (2010, 2012) and Dempsey et al. (2012). Dempsey et al. (2013) (hereafter, D13) present initial Flux Conversion Factors (FCFs; used to convert instrumental units to physical flux units) that were derived over the course of one year between 2011 and 2012 by observing standard sources, primarily Uranus. They found peak-flux calibration uncertainties of $\sim 14\%$ and $\sim 5\%$ at 450 and 850 μm , respectively. After nearly a decade of operation, thousands of calibrator observations have been obtained, increasing D13’s sample size by an order of magnitude. This dataset enables the robust study of trends in fluxes as a function of transmission and time of observation. Additionally, the influence of significant changes to the optical path resulting from hardware maintenance and improvement throughout SCUBA-2’s history can be addressed.

In the global context of astronomy undertaken at ~ 450 and ~ 850 μm , SCUBA-2’s flux calibration per-

formance is most naturally compared to other CCD-style bolometer arrays used by ground-based, single-dish telescopes. The first bolometer-array instrument was the Submillimeter High Angular Resolution Camera II (SHARC-II; Dowell et al. 2003) at the Caltech Submillimetre Observatory, situated approximately 150 meters from the JCMT near the summit of Maunakea. Operating at 350 and 450 μm , the flux-calibration uncertainty is quoted to be $\sim 30\%$ at both wavelengths (e.g. Marsh et al. 2006). SCUBA-2’s 850 μm band can be most directly compared to the Atacama Pathfinder Experiment’s (APEX) 870 μm bolometer array known as the Large Apex BOLometer CAmera (LABOCA) (Kreysa et al. 2003). The flux-calibration uncertainty for this instrument has been determined to be $\sim 15\%$, (e.g. Schuller et al. 2009). The Green Bank Telescope’s new Multiplexed Squid TES Array at Ninety Gigahertz-2 (MUSTANG-2; Dicker et al. 2014) operates at ~ 3.3 mm. While more distant in terms of wavelength, this instrument still provides a useful point of comparison. Its quoted flux uncertainty is $\sim 10\%$ (e.g. Ginsburg et al. 2020), an improvement over the previous MUSTANG array (Dicker et al. 2009), which had a systematic flux uncertainty of $\sim 20\%$ (e.g. Hughes et al. 2012). Most recently, beginning with The Next Generation Balloon-borne Large Aperture Submillimeter Telescope (BLAST-TNG, Lourie et al. 2018), arrays of Kinetic Inductance Detectors (KIDs) are now being deployed for submillimeter/millimeter observations. At the time of writing, the most direct comparison between a KID array and SCUBA-2 can be drawn between the Institut de Radioastronomie Millimétrique (IRAM) 30 m telescope’s “New IRAM Kids Arrays 2” (NIKA2, Calvo et al. 2016). NIKA2 is a dual-band millimetre continuum camera of operating at ~ 1 and 2 mm wavelengths. The initial rms calibration uncertainty is found to be 6%, based on 264 scans of point-like sources with flux density > 1 Jy at 1mm (Perotto et al. 2020), the waveband closest to SCUBA-2’s longest wavelength. Future comparisons with the Large Millimeter Telescope’s (LMT) TolTec (Lunde et al. 2020) KID instrument will also be performed.

In this paper, we present a historical record of the SCUBA-2 FCFs and their uncertainties from 2011 May 1 (beginning of on-sky commissioning dataset) to 2021 February 10, updating the calibration factors to be used when analyzing both archival or new SCUBA-2 data. In Section 2, we present a summary of the observations and data-reduction methods employed throughout this analysis. In Section 3, we discuss the conversion of the monitored opacity of the atmosphere at 225 GHz (τ_{225}) to the opacity at the wavelengths to which SCUBA-2

is sensitive in order to correct for telluric extinction. In Section 4 we report the recommended FCF values to use for the calibration of SCUBA-2 data obtained during the stable part of the night (07:00–17:00 UTC, 21:00–07:00 HST) depending on the date the data were observed. In Section 5, we present corrections to the standard FCFs for observations obtained outside the stable portion of the night, when the telescope dish is unstable to contraction and expansion due to changing temperature gradients in the support beams with the setting and rising of the Sun. In Section 6, we update the submillimeter fluxes of the most frequently used secondary calibrators, CRL 2688, CRL 618, Arp 220, and HL Tau based on the new calibration results. In Section 7 we apply the new results to nearly a decade of 850 μm observations of Quasar 3C 84 and compare the light curve with data obtained by the Submillimeter Array (SMA) and the Atacama Large Millimeter/Submillimeter Array (ALMA) as a case study. Finally, in Section 8 we provide a summary.

2. OBSERVATIONS AND DATA REDUCTION

SCUBA-2 obtains continuum data at 450 and 850 μm simultaneously with beam sizes of 10.0'' and 14.4'', respectively (see D13, Chapin et al. 2013, and Section 5.1 for more information). All observations that are used in this work were performed using the “CV Daisy” scan pattern which yields a $\sim 12'$ diameter map with a central 3' region exhibiting a highly uniform sensitivity (see Holland et al. 2013, for details). This scan pattern is ideal for recovering compact structures and it is used for both flux calibrator and science observations.

All the data were reduced using the iterative map-making software, MAKEMAP (Chapin et al. 2013), which is part of Starlink’s (Currie et al. 2014) Submillimetre User Reduction Facility (SMURF) package (Jenness et al. 2013). The default recipe for bright, compact sources was employed in order to robustly recover each calibrator. In order to achieve this, structures larger than 3.3' are spatially filtered and low-frequency noise is removed. To suppress the ringing introduced by such a high-pass filter, the map is constrained to zero beyond a radius of 1' from the source centre (significantly outside the power received by the beam’s central lobe) on all iterations but the last. A pixel size of 1'' was chosen for both the 450 and 850 μm final maps.

The first SCUBA-2 calibrator observations addressed by this study were performed in 2011 May during the instrument’s commissioning phase. D13 analyzed the calibrator data taken over one year beginning on 2011 May 1 to derive the initial “Flux Conversion Factors” (FCFs; see Section 4 for details), beam profiles, and

secondary-calibrator brightnesses. Now, we continue the analysis through 2021 February 10.

Over the course of 10 years, more than 1200 reliable observations of the primary calibrator, Uranus, alone have been obtained. Together with the secondary calibrators, this is a sufficient amount of data to probe changes in the measured calibrator fluxes as a function of atmospheric transmission, UTC date, and UTC time (hour of night). The UTC-date analysis reveals significant changes to the measured fluxes due to changes in hardware, while the UTC time highlights patterns in dish settling and expansion with the ambient temperature. Early in the evening and after the Sun has risen in the morning, the JCMT dish experiences significant temperature gradients that affect its shape and, consequently, the calibration (see Section 5 for more details).

Only observations that achieved a signal-to-noise ratio (SNR) of at least 4 were included in the analysis to ensure an accurate fit could be made to peak flux of the calibrator source. The 450 μm data are much more sensitive to wet weather than their 850 μm counterparts, so there are fewer usable observations at 450 μm in these conditions. “Evening” observations, when dish settling is expected, takes place between 03:00 and 07:00 UTC (17:00 and 21:00 Hawaii-Aleutian Standard Time, HST). “Night” observations, when observations are expected to be most stable, take place between 07:00 and 17:00 UTC (21:00 and 07:00 HST). “Morning” observations, when dish expansion is expected, are typically undertaken during “Extended Observing” time, 17:00 to 22:00 UTC (07:00 to 12:00, HST). Extended Observing began in October, 2013. Even before all JCMT observations were carried out remotely beginning 2019 November 1 (Parsons et al. 2020), the telescope was always operated remotely from sea level during Extended Observing with the “handover” taking place between 16:00 and 18:00 UTC.

3. EXTINCTION CORRECTION: OPACITY RELATIONS

The default data-reduction scheme calculates an atmospheric extinction correction for each observation based on the airmass and the amount of precipitable water vapor (PWV) along the line of sight (the opacity of the atmosphere is used as a proxy for the PWV). The correction assumes an initial signal, I_0 , is exponentially attenuated as follows,

$$I_0 = \frac{I_m}{\exp(-\tau_{\nu,\text{zen}}A)}, \quad (1)$$

where I_m is the measured signal, $\tau_{\nu,\text{zen}}$ is the zenith opacity of the atmosphere at the observed frequency ν ,

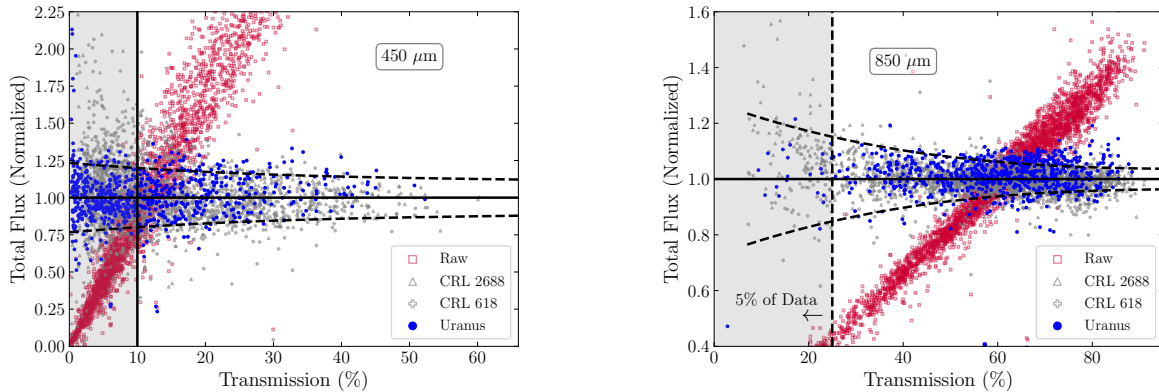


Figure 1. Normalized raw (no atmospheric extinction correction applied) total-flux measurements of Uranus, CRL 2688, and CRL 618 as a function of transmission are shown as red squares. The atmospheric-extinction corrected peak fluxes are overlaid with the primary calibrator, Uranus, shown in blue (circles) and the secondary calibrators CRL 2688 and CRL 618 shown in gray (triangles and pluses, respectively). The applied extinction correction uses the opacity relations of the form presented in Equation 6 with coefficients detailed in Table 1. Dashed lines represent the measured median absolute deviation in the data in ten evenly spaced transmission bins. The corrected calibrator fluxes are approximately flat across the range of atmospheric transmissions at which the JCMT operates, correcting for the increased signal attenuation seen in the raw data at higher transmissions. *Left:* 450 μm . The vertical dashed line represents a transmission of 10%, below which a negligible amount of 450 μm data can be used due to low signal to noise (grayed region). *Right:* 850 μm . The vertical dashed line represents a transmission of 25%, marking the 5% of observed data that begins to have a significantly larger scatter than their higher transmission counterparts (grayed region).

and A is the airmass of the source. Equation 1 assumes a plane-parallel atmosphere and an opacity that is independent of the frequency across the filter profile. The expression in the denominator:

$$\exp(-\tau_{\nu,\text{zen}} A) \quad (2)$$

is defined as the *atmospheric transmission* (hereafter, *transmission*). Therefore, the derivation of an accurate correction depends on how closely the atmosphere resembles the plane-parallel assumption and how well $\tau_{\nu,\text{zen}}$ can be measured.

A water-vapor monitor (WVM) operating at 183 GHz is mounted in the JCMT receiver cabin, obtaining measurements every 1.2 seconds via a pick-off mirror. The WVM measures three brightness temperatures at frequencies sampling the wings of the prominent 183 GHz water line. Fitting the properties of the water line allows for a conversion to the amount of PWV that is present along the line of sight during an observation (see [Wiedner 1998](#), for details on the WVM). The measured PWV is converted to its zenith value, PWV_{zen} , by dividing by the airmass, so it can be directly related to the zenith opacity at 225 GHz, $\tau_{225,\text{zen}}$ (D13),

$$\tau_{225,\text{zen}} = 0.04 \times \text{PWV}_{\text{zen}} + 0.017. \quad (3)$$

The reason for this conversion is historical: it allows direct comparison with the fixed-azimuth 225 GHz tipping radiometer formerly situated at the Caltech Submillime-

ter Observatory (CSO). In 2015, however, the CSO radiometer was hit by a falling piece of ice, which had the effect of shifting the measured opacity to generally lower values than measured at the JCMT with no consistent systematic trend¹. In 2015 October, it was moved from the CSO site (150 meters southeast of the JCMT) to the Submillimeter Array site (100 meters northwest of the JCMT).

In order to perform a reliable extinction correction, a conversion must be made from $\tau_{225,\text{zen}}$ to $\tau_{666,\text{zen}}$ and $\tau_{345,\text{zen}}$, corresponding to the observing frequencies of SCUBA-2 (450 μm = 666 GHz and 850 μm = 345 GHz). D13 report opacity relations of

$$\tau_{666,\text{zen}} = 26.0 \times (\tau_{225,\text{zen}} - 0.012) \quad (4)$$

$$\tau_{345,\text{zen}} = 4.6 \times (\tau_{225,\text{zen}} - 0.0043) \quad (5)$$

based on one year of data obtained beginning in 2011 May.

To test these opacity relations on the larger 10-year data set, a more general form of the opacity relation was defined to include a higher-order term, expecting a deviation from linearity. It was found that a square-root dependence produces a marginally flatter flux response

¹ See The Submillimeter Array Memo 164, Radford, S. <https://lweb.cfa.harvard.edu/sma/memos/164.pdf>

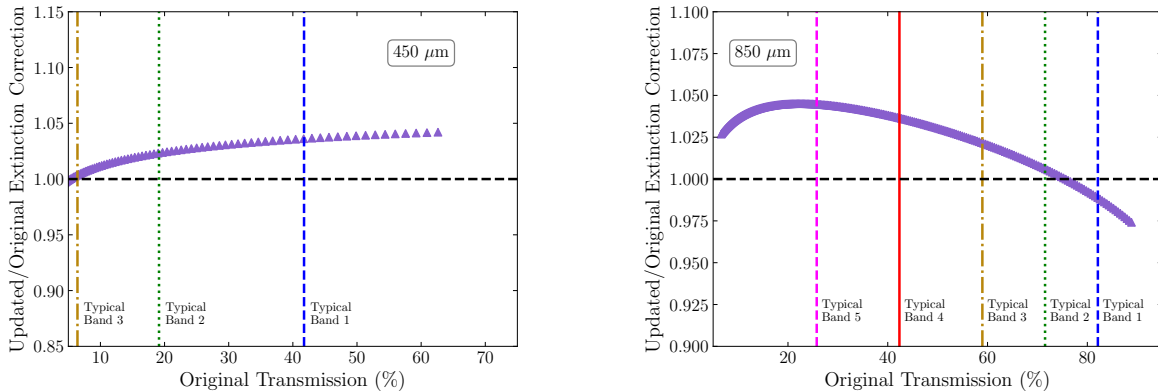


Figure 2. The newly derived extinction correction (the reciprocal of Equation 2 using the opacity relations presented in Equation 6 with coefficients presented in Table 1) divided by the original extinction correction (the reciprocal of Equation 2 using opacity relations presented in Equations 4 and 5) as a function of atmospheric transmission. Vertical lines show the transmission of the typical JCMT weather bands at each wavelength, assuming an airmass of 1.2. *Left:* 450 μm . *Right:* 850 μm . At 450 μm , the original opacity relation is modified by a maximum factor of 5% in very dry weather while at 850 μm the original opacity relation is modified by a maximum factor of 3–4% in very dry or very wet conditions. The majority of 850 μm observations, however, require no modification from the original results presented by D13.

Table 1. Opacity relation coefficients corresponding to Equation 6.

Coefficient	450 μm	850 μm
a	23.3 ± 1.5	3.71 ± 0.18
b	-0.018 ± 0.006	-0.040 ± 0.008
c	0.05 ± 0.04	0.202 ± 0.044

as a function of transmission when compared with Equations 4 and 5, especially when the atmosphere is highly opaque. The form of the updated opacity relation is

$$\tau_{\nu,\text{zen}} = a \times (\tau_{225,\text{zen}} + b + c \times \sqrt{\tau_{225,\text{zen}}}), \quad (6)$$

where a , b , and c are fitted parameters. Using the raw, *uncorrected* peak flux measurements (I_m , Equation 1) of the three most-used calibrator sources: Uranus, CRL 2688, and CRL 618, along with the airmass at the time of each observation, the optimal parameters (a , b , c) were derived by minimizing the variance in the normalized² *corrected* peak flux (I_0 , Equation 1) versus transmission curve. The minimization routine used was the Broyden-Fletcher-Goldfarb-Shanno (BFGS) algorithm, employed by SCIPY’s OPTIMIZE.MINIMIZE function in the Python programming language³. The fi-

nal parameters and associated uncertainties are derived by bootstrapping the minimization over 1000 iterations, during which random perturbations are added to the residual between the normalised corrected flux and a value of 1.0. The perturbations were generated by drawing random values from a normal distribution with a standard deviation equivalent to the standard deviation of the original set of residuals. Before the minimum variance was calculated, the flux values were averaged over τ_{225} bins of width 0.01 and airmass bins of 0.1. The binning was performed in order to mitigate the effect of highly sampled areas of parameter space dominating less-sampled areas, causing poor fits for conditions in which fewer observations are performed. In this way, the flux values used to fit a , b , and c represent the best knowledge of the behavior of each particular region of the parameter space. Times during which the JCMT WVM was behaving abnormally, the protective GORE-TEX™ membrane⁴ was removed from the telescope, or the secondary mirror was malfunctioning were not considered in the analysis (see Section 4).

Throughout the history of SCUBA-2, the opacity relations at both 450 and 850 μm remain consistent with (a , b , c) coefficients corresponding to Equation 6 presented in Table 1.

Figure 1 shows the normalised raw flux measurements of Uranus, CRL 2688, and CRL 618 as a function of

² The measured peak fluxes of Uranus were normalised to the varying, expected brightness of the planet on each observation date to take into account seasonal flux changes.

³ <https://docs.scipy.org/doc/scipy/reference/generated/scipy.optimize.minimize.html>

⁴ In order to shield the telescope and sensitive electronics from wind and dirt, the JCMT is covered by a GORE-TEX™ membrane that is transparent at submillimeter/millimeter wavelengths.

Table 2. Weather band to PWV conversion.

Weather Band ^a	$\tau_{225,zen}^b$	PWV ^c (mm)
1 (Typical)	0.04	0.58
1/2 Boundary	0.05	0.83
2/3 Boundary	0.08	1.58
3/4 Boundary	0.12	2.58
4/5 Boundary	0.20	4.58

NOTE—^aThe JCMT classifies 5 different “weather bands” according to the amount of precipitable water vapor in the atmosphere.

^bThe zenith opacity of the atmosphere at 225 GHz (see Equation 3).

^cPrecipitable water vapor.

transmission (red squares) overlaid by the corrected fluxes after applying the extinction correction that is calculated using these new opacity relations. The result is a consistent flux response across the full range of transmissions typically used during observations. Vertical, dashed lines at 10% and 25% for 450 and 850 μm data, respectively, highlight transmissions below which the opacity relations become significantly more uncertain. In the case of the 850 μm relation in the very poor transmission regime, the secondary calibrators show evidence of an over-correction (see also Appendix A). At 450 μm , a transmission of $\leq 10\%$ occurs when observing at an elevation at or below 42° (Airmass = 1.5) in typical JCMT Weather Band 2 conditions ($\tau_{225,zen} = 0.065$; see Table 2). In the case of 850 μm , a transmission of 25% occurs when observing at an elevation of 42° (Airmass = 1.5) at the border of Weather Band 4/5 ($\tau_{225,zen} = 0.2$), or when observing at an elevation of 30° (Airmass = 2.0) at a Weather Band 4 opacity of $\tau_{225,zen} = 0.15$. In Weather Bands 1, 2, or 3, the 850 μm transmission is always higher than 25% (less than 5% of SCUBA-2 science data is obtained below this threshold).

In Figure 2, the extinction correction using the newly derived opacity relations (Equation 6) is directly compared with the original extinction correction using the opacity relations derived in D13 across the observable transmission range. As expected, the 450 μm data have a high enough transmission to be analyzed only in Weather Bands 1 and 2, while wetter weather quickly renders peak-flux measurements less certain. The new extinction correction produces fluxes that are 2–5% higher than the original factor yields depending on the transmission, with the largest factor affecting the driest weather observations, which were previously under-

corrected. At 850 μm the peak-flux measurements are robust in all weather bands. The new extinction correction modifies the 850 μm flux by a maximum of 3–4% at atmospheric transmissions above 25%. The largest differences to data occur in the extremes of the wettest and driest weather which were previously under and over-corrected, respectively. The majority of 850 μm data has a negligible change ($< 3\%$) in corrected flux when using the new opacity relations.

4. FLUX CONVERSION FACTORS (FCFS)

After flat-fielding, raw data obtained by SCUBA-2 initially have units of picowatts (pW; see Chapin et al. 2013). After an atmospheric-extinction correction is applied (see Section 3), a conversion must be made to flux units. There are two types of “Flux-Conversion Factors” (FCFs) that can be applied depending on a project’s scientific motivation.

1. Peak FCF (FCF_{peak}): Also known as “Beam FCF”, this factor converts every pixel in a map from pW into Jy beam^{-1} (with units of $\text{Jy beam}^{-1} \text{pW}^{-1}$). This is useful when peak fluxes of discrete point-source objects are being measured. The brightest pixel in the source represents the flux in Jy distributed over the full area of the beam. To calculate the Peak FCF, we fit the calibrator source with a two-dimensional Gaussian function using CUPID’s (Berry et al. 2013) GAUSSCLUMPS (Stutzki & Guesten 1990) program, found in the Starlink software suite (Currie et al. 2014), to measure the raw peak brightness, $I_{\text{m,peak}}$ (in units of pW). We then compare the result with the modeled peak flux of the source, S_{peak} , (in units of Jy beam^{-1}),

$$\text{FCF}_{\text{peak}} = \frac{S_{\text{peak}}}{I_{\text{m,peak}}}. \quad (7)$$

2. Arcsecond FCF ($\text{FCF}_{\text{arcsec}}$): Also known as the “Aperture FCF”, this factor converts every pixel in a map from pW to Jy arcsec^{-2} (with units of $\text{Jy arcsec}^{-2} \text{pW}^{-1}$). This conversion factor is necessary when measuring the total flux of extended emission structures. To calculate the Arcsecond FCF, we first measure the total flux in pW, $I_{\text{m,total}}$, by integrating over a $60''$ diameter aperture centered on the calibrator source and subtracting a background level averaged over an annulus with inner radius $90''$ and outer radius $120''$. We then compare the result with the modeled total flux of the calibrator source, S_{total} (in units of Jy), dividing by the area of a pixel, A_{pix} , in units

of arcsec²,

$$\text{FCF}_{\text{arcsec}} = \frac{S_{\text{total}}}{I_{\text{m,total}} \times A_{\text{pix}}} \quad (8)$$

Note that the pixel area of the calibrator maps is 1 arcsec². Additional tests have been performed at different pixel sizes and the resulting $\text{FCF}_{\text{arcsec}}$ value remains consistent for maps with pixels of side length between 1–4''.

For a true point source, the measured peak pixel of a source in a map calibrated in units of Jy beam⁻¹ is equivalent to the integrated total flux of the same source in a map calibrated in units of Jy (correcting for the pixel size in arcseconds).

In the following section, the FCF distributions and the associated uncertainties of the primary calibrator source Uranus are analyzed as a function of date to determine significant historical impacts on SCUBA-2's optical path. The recommended FCFs to use on data obtained during the stable part of the night (07:00–17:00 UTC) are presented in Table 4 and corrections to these values for data obtained outside of these times are given in Section 5 and Table 5.

An additional correction is required when applying a matched-filter⁵ to data. A matched filter is applied when seeking to optimally identify and characterize sources that are the size of the telescope beam, suppressing residual large-scale noise:

*When a matched filter is applied to the data, the **Peak FCFs** presented in Table 4 must be reduced by 2%*⁶.

Additional correction factors to the FCFs presented in the sections below are also required when the POL-2 instrument is in use. This is largely due to the reduced optical throughput caused by the introduction of a spinning wave-plate.

*All **FCFs** presented in Table 4 must be multiplied by 1.96 and 1.35 at 450 and 850 μm , respectively, when POL-2 is in use.*

4.1. FCFs as a Function of Date

Figure 3 and Table 3 show the derived FCFs as a function of date using the primary calibrator Uranus⁷.

Uranus's flux model is well-known (to within 5%; Orton et al. 2014) and it produces flat, stable light curves when corrected by the opacity relations described above in Section 3. All observations included in the figure were obtained in the most stable part of the night, 07:00–17:00 UTC, in order to avoid effects introduced by the changing shape of the dish as it cools in the evening and warms in the morning (see Section 5). Gray shaded regions, from earliest to latest (left to right in the figure), show two intervals during which there was no reliable WVM to indicate the amount of water-vapor extinction along the line of sight, one interval during which the GORE-TEX™ membrane was removed for POL-2 commissioning, and one interval during which the Secondary Mirror Unit (SMU) was malfunctioning (see Section 4.1.1).

Large outliers in the FCF distributions are biased to higher values and correspond to focus issues or pixel-to-pixel noise that causes the Gaussian fit to underestimate the true peak brightness of the source. Derived FCFs for each calibrator were deemed robust provided a peak flux could be reliably fit using a Gaussian profile. Transmission lower limits of 10% and 25% have also been applied to the 450 and 850 μm data, respectively (see Section 3).

Table 4 presents the recommended FCFs for observations obtained during the stable part of the night (07:00–17:00 UTC) as a function of the observation date. The FCF value before and after each significant shift in the flux (Figure 3, see text below for details) is represented by the median value of Uranus's FCF distribution. The typical uncertainty, likewise, is represented by the median absolute deviation (MAD) of the FCF distribution added in quadrature with the uncertainty in Uranus's flux model (5%). To verify the results, the secondary calibrator source that is observed most often, CRL 2688, was analysed in the same manner and there is no significant difference between the derived FCFs (see Section 6 for further information on the secondary calibrators).

The Peak FCF distributions have uncertainties of 17% and 7% at 450 and 850 μm , respectively. Both values are slightly higher than the previously derived 14% at 450 μm , and 5% at 850 μm (D13). The Arcsecond FCFs have uncertainties of 14% and 6% at 450 and 850 μm , respectively; these are also both slightly larger than the previously derived 11% and 3% derived by D13. The smaller uncertainties at 850 μm when compared with the 450 μm regime is due to the higher transmission and stability of the submillimeter atmosphere. A full analysis of the inherent scatter in the FCF distributions is beyond the scope of this paper, though a discussion is offered in Appendix A.

⁵ See Appendix D of the SCUBA-2 Data Reduction Cookbook for detailed information: <https://starlink.eao.hawaii.edu/docs/sc21.pdf>

⁶ See <https://www.eaoobservatory.org/jcmt/instrumentation/continuum/scuba-2/calibration/> for current SCUBA-2 calibration information.

⁷ The full table is available in the online version.

Table 3. Uranus-derived FCF Information*

MJD	τ_{225}^a	A^b	450 μm Peak FCF ^c (Jy pW ⁻¹ beam ⁻¹)	450 μm Arcsec FCF ^d (Jy pW ⁻¹ arcsec ⁻²)	850 μm Peak FCF ^c (Jy pW ⁻¹ beam ⁻¹)	850 μm Arcsec FCF ^d (Jy pW ⁻¹ arcsec ⁻²)
...
56088.6892	0.066	1.085	515.80	4.91	503.46	2.25
56102.7249	0.054	1.066	732.73	5.51	547.90	2.35
56103.7297	0.054	1.077	528.94	4.92	506.83	2.27
56105.5995	0.041	1.221	495.46	4.55	515.29	2.25
56105.7215	0.043	1.073	535.79	4.88	510.93	2.27
56109.7449	0.048	1.153	645.76	4.53	551.56	2.30
56109.6842	0.050	1.048	599.89	4.71	543.25	2.30
56110.5168	0.043	1.859	403.92	3.80	531.33	2.27
56110.6040	0.046	1.151	402.80	3.99	494.46	2.22
56112.5498	0.046	1.408	488.38	4.36	539.04	2.31
...

NOTE—^aThe opacity of the atmosphere at 225 GHz at the time of the observation.

^bThe airmass at the time of the observation.

^cPeak fluxes were measured by performing a Gaussian fit to the source while the data was still in units of picowatts. These measurements were then compared to the expected (model) peak flux of Uranus at the time of observation.

^dTotal fluxes were measured using aperture photometry while the data was still in units of picowatts. The total flux was calculated within a 1 arcminute diameter aperture centered on the source. The background level was determined using an annulus with inner diameter 1.5 arcminutes and outer diameter 2 arcminutes. These measurements were then compared to the expected (model) total flux of Uranus at the time of observation.

* The full table is available in the online version.

Table 4. Recommended FCFs for observations obtained between 07:00-17:00 (UTC).

Wavelength, Date Range	FCF _{peak}	FCF _{arcsec}
450 μm , Pre 2018 Jun 30	531 \pm 93	4.61 \pm 0.60
450 μm , Post 2018 Jun 30	472 \pm 76	3.87 \pm 0.53
850 μm , Pre 2016 Nov 19	525 \pm 37	2.25 \pm 0.13
850 μm , 2016 Nov 19 to 2018 Jun 30	516 \pm 42	2.13 \pm 0.12
850 μm , Post 2018 Jun 30	495 \pm 32	2.07 \pm 0.12

NOTE—These FCFs assume the opacity relations presented in Equation 6 and Table 1 were applied during the extinction correction. The same extinction correction must be used for a direct comparison with the FCF values presented by D13. The atmospheric transmission lower limits included in the FCF determination are 10% and 25% for 450 and 850 μm , respectively. The primary calibrator, Uranus was used to derive these FCFs.

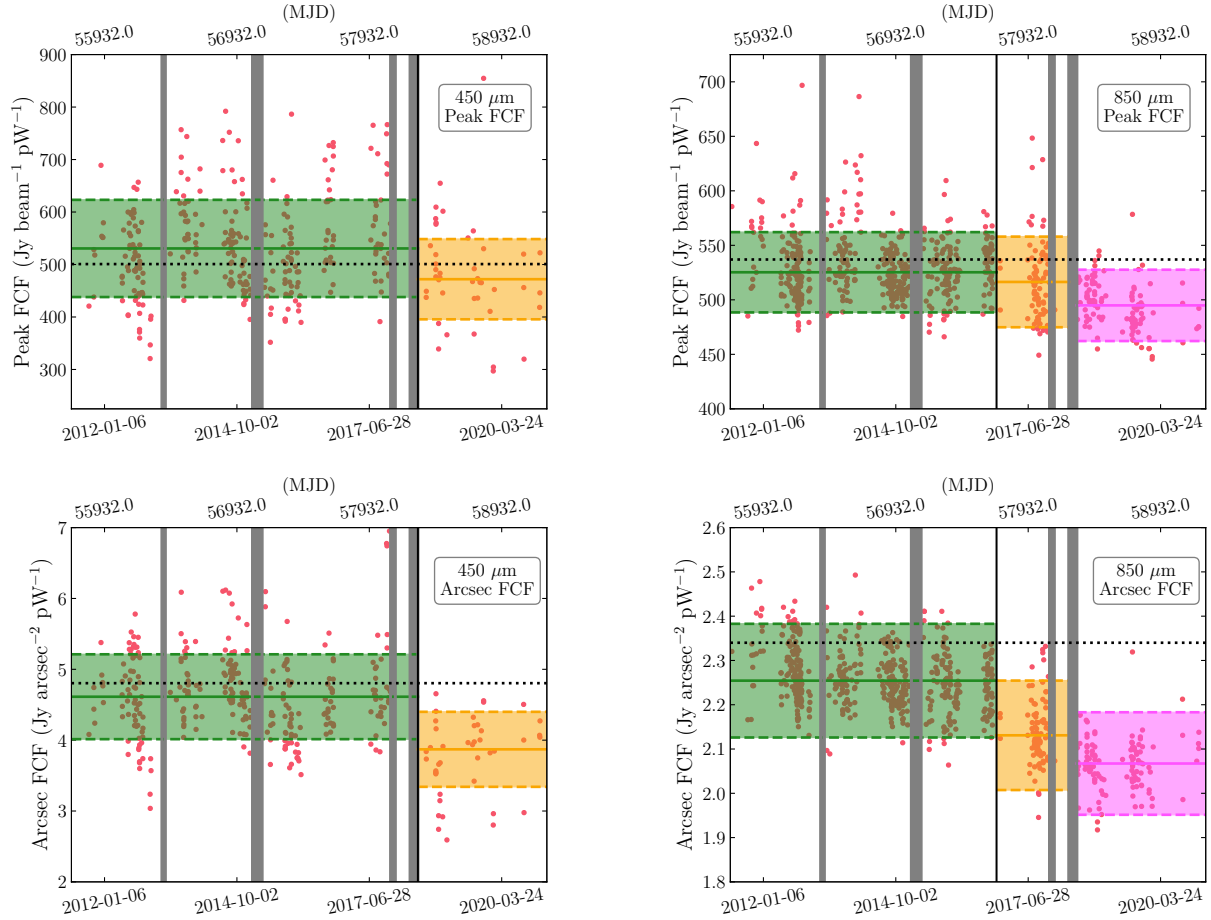


Figure 3. Flux conversion factors (FCFs) derived using flux measurements of the primary calibrator Uranus during the stable part of the night (07:00-17:00 UT) as a function of date. The gray shaded regions indicate epochs that are not included in the FCF determinations. The earliest two excluded time intervals indicate when there was no reliable WVM obtaining data from the JCMT. The third interval indicates when the GORE-TEX™ membrane was removed from the telescope for POL-2 commissioning. The latest excluded interval indicates the time when the secondary mirror was malfunctioning (see Section 4.1.1). The horizontal, shaded regions indicate the median FCF value over each span of time and the associated median absolute deviation added in quadrature with the 5% uncertainty in the Uranus flux model. The black (dotted) lines indicate the original FCF value derived by D13, adjusted for the newly derived opacity relation, assuming the most common atmospheric transmissions during observations (see Figure 2). The recommended FCFs to apply to observations obtained in the stable part of the night are summarised in Table 4. *Left:* Peak (*Top*) and Arcsecond (*Bottom*) FCFs derived at 450 μm . The solid, vertical line at the right edge of the latest gray region marks 2018 June 30, when the secondary-mirror malfunction was fixed. Data wherein the atmospheric transmission are less than 10% are excluded. *Right:* Peak (*Top*) and Arcsecond (*Bottom*) FCFs derived at 850 μm . The solid, vertical line marks 2016 November 19 when the SCUBA-2 thermal filter stack was updated. Data wherein the atmospheric transmission are less than 25% are excluded.

At $450\ \mu\text{m}$, there is a single downward shift in FCF values. The shift occurs on 2018 June 30 (solid black vertical line on the right edge of the latest gray region in left panels of Figure 3) after heavy SMU maintenance was performed wherein:

1. The mirror was cleaned;
2. The accuracy of the Y-Axis Linear displacement Variable Transducer (LDVT) was significantly improved;
3. The chopper actuators that hold the SMU in the zero position were balanced;
4. The drive motor assemblies for each axis were disassembled, inspected, and improved both mechanically and electrically;
5. The mirror was re-centred in its position above the primary; and
6. The E-W chopper electronics were debugged after an intermittent issue with source aspect ratios became evident throughout the month of 2018 June (see Section 4.1.1 for more details).

The combination of these adjustments significantly improved the flux concentration. This decrease in beam dilution translates to an increase in flux and a reduction in FCF values. The average $450\ \mu\text{m}$ Peak FCFs are reduced by 11% (top left panel of Figure 3). While the drop appears much more significant for the Arcsecond FCF values (bottom left panel of Figure 3), this is because the scatter in the light curves is significantly lower when compared with the Peak FCF values. Overall, the Arcsecond FCF trends at both wavelengths have less scatter and fewer outliers than their Peak FCF counterparts because they rely on aperture photometry and are, therefore, less affected by pixel-to-pixel noise and not affected by Gaussian-fitting uncertainties. Based on the $450\ \mu\text{m}$ Arcsecond FCF data, the downward shift in values is 16% (in agreement with the Peak FCF results within the derived uncertainties).

At $850\ \mu\text{m}$, the FCF values experienced two downward shifts. The first was on 2016 November 19 after new thermal-filter stacks were installed for each wavelength. The original 60 K, $37\ \text{cm}^{-1}$ Low-pass Edge (LPE) filter was replaced with a $55\ \text{cm}^{-1}$ LPE filter with an improved transmission profile in the $850\ \mu\text{m}$ observing band (Cookson et al. 2018). The main reason for the filter change was to lower the detector loading by reducing the temperature of the filters and not, necessarily, to improve the transmission. However, there is a 2% transmission improvement when measured using the

$850\ \mu\text{m}$ Peak FCF distributions and a 5% improvement when measured using the Arcsecond FCFs. No significant shift was expected or seen at $450\ \mu\text{m}$ after the 2016 November thermal-filter installation, as there was no improvement in the transmission profile of the new filter stack at this waveband. The second shift at $850\ \mu\text{m}$ occurs after the SMU maintenance described, above. Due to the large and more-stable beam profile when compared with $450\ \mu\text{m}$ (see Section 5.1), the magnitude of this downward shift is 4% when measured using the Peak FCFs and 3% when measured using the Arcsecond FCFs (in agreement to within the derived uncertainties).

4.1.1. Secondary-mirror Malfunction

Throughout 2018 May, the SMU underwent heavy maintenance wherein it was removed from the telescope (see Section 4.1). For several weeks after, until 2018 June 30, there was an intermittent issue with the East-West (E-W) chopper that resulted in the elongation of compact sources, mainly affecting the Peak-FCF measurements during this time. While “chopping” is not performed during SCUBA-2 observing, the electronics that control the chopper are responsible for keeping the observation at a fixed angle throughout the observations. Therefore, any oscillation in the electronics affect the SMU position and the FCFs. The top panels of Figure 4 show the aspect ratio of Uranus and CRL 2688 plotted as a function of UTC date. The time interval of the intermittent problem can be clearly seen as a spike in the aspect ratios⁸. Engineering/commissioning telescope time was specifically used to observe the secondary calibrator source CRL 2688 in the time following the SMU maintenance, which is why the number of observations is relatively high.

The bottom panels of Figure 4 show the FCFs derived during the stable part of the night using CRL 2688 before, during, and after the SMU malfunction. Note that throughout the duration of the intermittent problem, several FCFs indicated the system was performing within normal parameters. Once the E-W chopper was fixed (2018 June 30), the SMU maintenance of 2018 was complete and, as noted previously, there was an improvement in flux concentration within the beam. There have been no further issues with the data as a result of the SMU since 2018 June 30. While the main science programs being carried out during 2018 May were checked to ensure that the quality of the produced maps was not adversely affected, science data (especially point

⁸ Errant aspect ratios can also occur due to low-signal-to-noise observations when the 2D Gaussian fit is less certain.

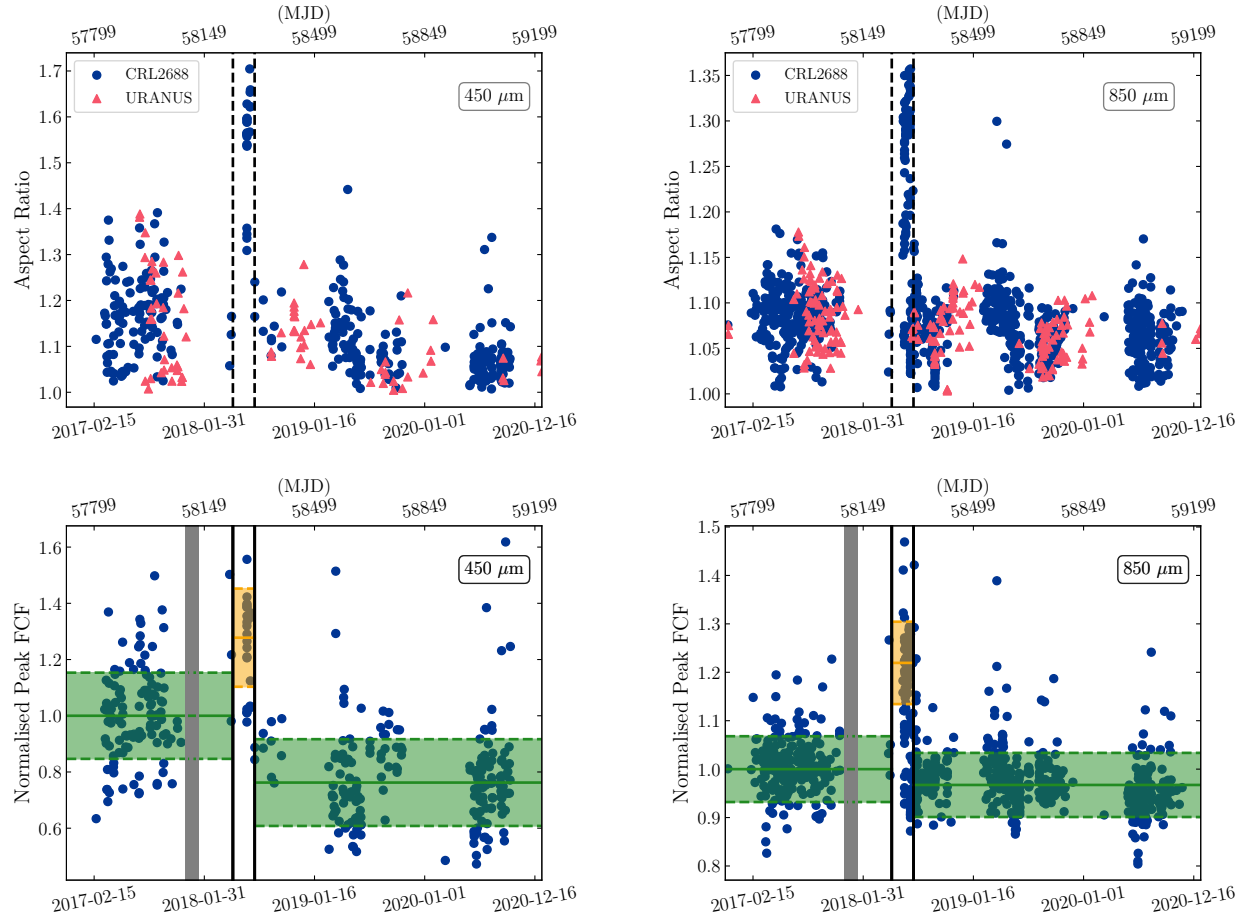


Figure 4. *Top:* 450 (*left*) and 850 μm (*right*) aspect ratios of CRL 2688 (circles) and Uranus (triangles) observations as a function of date derived by fitting the calibrators with a 2D Gaussian function. The vertical, dashed lines indicate the time interval of the secondary-mirror malfunction, correlating with large aspect ratios. *Bottom:* Normalized 450 (*left*) and 850 μm (*right*) Peak FCFs derived using flux measurements of the secondary calibrator CRL 2688 throughout the stable part of the night (0700–1700 UTC) as a function of date. The gray shaded region indicates when the GORE-TEX™ membrane was removed from the telescope for POL-2 commissioning. The two solid, vertical lines mark the time interval in which the secondary-mirror was malfunctioning. The horizontal, shaded regions indicate the median FCF value over each span of time and the associated median absolute deviation. Point source observations observed during June 2018 should be carefully inspected before use.

sources) obtained during this period should be carefully examined before use.

5. FCF NIGHTLY PATTERNS

It is well known that the temperature decrease and increase in the early evening and late morning, respectively, causes slight structural changes to the dish that can affect the beam shape, focus and, ultimately, the calibration. In Figure 5, we present the derived, normalized FCFs as a function of time of night. All Uranus and CRL 2688 observations taken when the atmospheric transmission was greater than 10% at 450 μm and 25% at 850 μm since 2011 May are included in the figure. The same trends are observed both before and after the key dates when the FCFs shifted (Section 4.1).

In the top panels of Figure 5, there is an obvious U-shape in the nightly Peak FCF data that corresponds to dish instability. The vertical lines in each figure are drawn at 07:00 UTC (21:00 HST) and 17:00 UTC (07:00 HST), marking when the dish is stable to dynamic deformations. The 450 μm data show a more dramatic trend in FCFs as its beam profile is more sensitive than its 850 μm counterpart to atmospheric and structural effects. Without accounting for the obvious increase in Peak FCFs in the evening and morning observing regimes, the uncertainties for a typical calibrator source at 450 μm varies from 20% in the evening to 17% during the night, and it can reach up to 25% in the morning. At 850 μm , the Peak FCF uncertainties in each source distribution are 8% in the evening, 7% during the night, and up to 10% in the morning. In the day time, uncer-

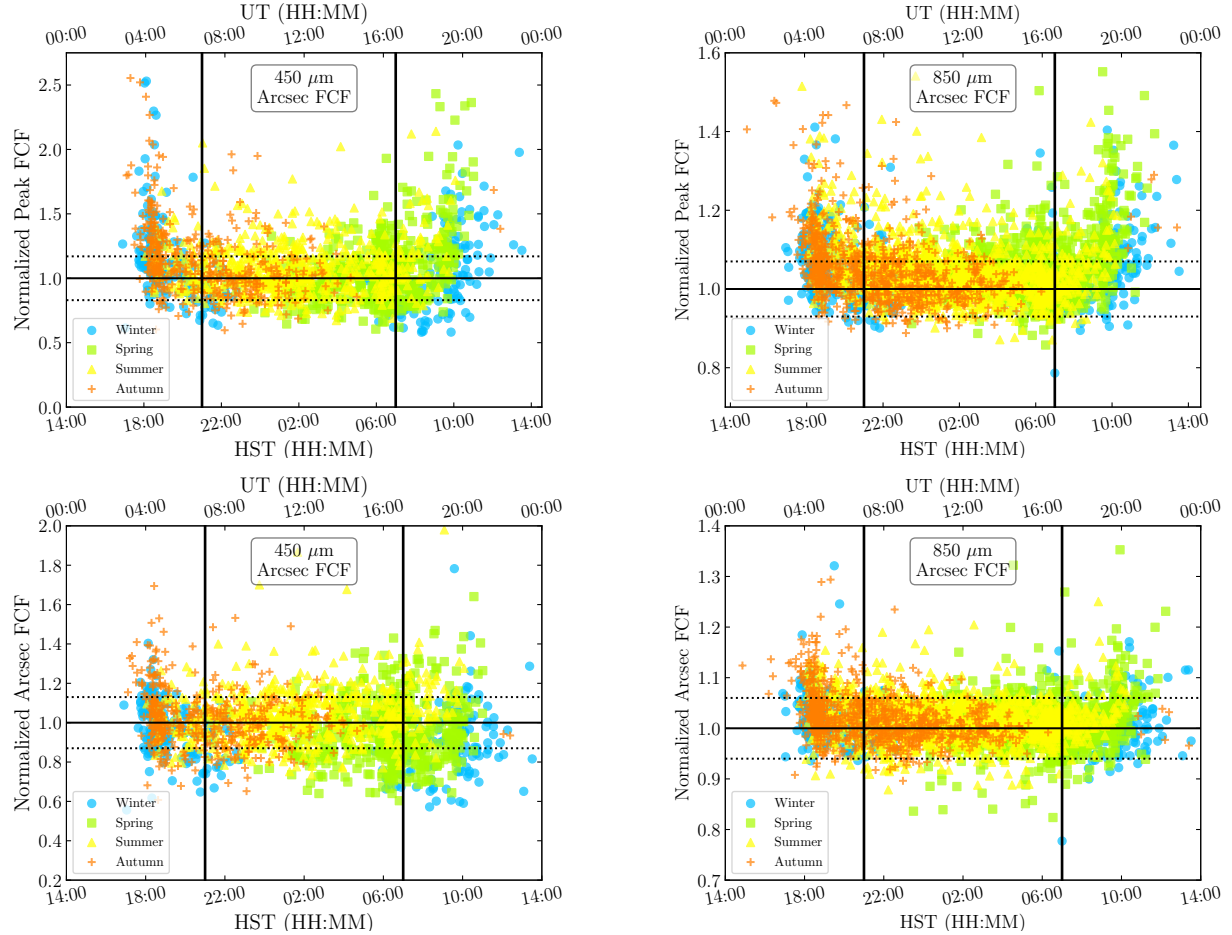


Figure 5. Normalized Peak (*top*) and Arcsecond (*bottom*) FCFs at 450 (*left*) and 850 μm (*right*) as a function of observation time. All FCFs are derived using the primary calibrator Uranus and secondary calibrator CRL 2688. The results presented in Table 4 were used for the normalization. No data are included for the periods in which there were no reliable JCMT WVM data, the GORE-TEXTM membrane was removed, or the secondary mirror was malfunctioning (see Figure 3). The vertical lines mark the beginning and end of the stable observation period from 07:00–17:00 (UTC). The horizontal (dotted) lines show the FCF uncertainties derived for the stable observation period around a value of 1.0 (horizontal, solid line). Data are colored according to season: blue circles represent Winter, green squares represent Spring, yellow triangles represent Summer, and orange crosses represent Autumn. There are no significant trends with the time of year. The early-evening and late-morning Peak FCF observations deviate significantly from the stable observations, while the Arcsecond FCFs remain largely unchanged with a small increase in the uncertainty in the evening and morning.

tainties in the observations are dominated by the ambient temperature increase and air stability decrease (seeing) when compared to night observations. In the afternoon, the opening of the dome typically causes a faster temperature decrease and hence more thermal deformations. As expected, the Arcsecond FCFs (bottom panels of Figure 5) show a much weaker nightly trend as the large-aperture photometry used to calculate these values is more stable to beam deformation than the Gaussian fits used to derive the Peak FCFs. With a 60'' diameter aperture used for the photometry, only the secondary (“error”) beam is affected (see Section 5.1), which has a small effect on the data at all transmission bands of interest. The 450 μm Arcsecond FCF uncertainties range

from 17% in the evening and morning to 14% in the stable part of the night, while the 850 μm Arcsecond FCF uncertainties range from 6% in the stable part of the night to 7% in the evening and morning.

Figure 6 shows the Peak FCF trends in detail for evening, night, and morning observations of Uranus and CRL 2688. In the evening, between 03:00 and 07:00 (UTC), a first-order correction to the instability in the Peak FCFs caused by the settling dish can be derived by bootstrap-fitting (1,000 iterations) a linear function of the relative Peak FCF values over time. Such a correction indicates the Peak FCFs decrease at rates of $9.1 \pm 0.5\% \text{ hr}^{-1}$ and $3.2 \pm 0.1\% \text{ hr}^{-1}$ at 450 and 850 μm , respectively. This is due to the peak flux increasing as

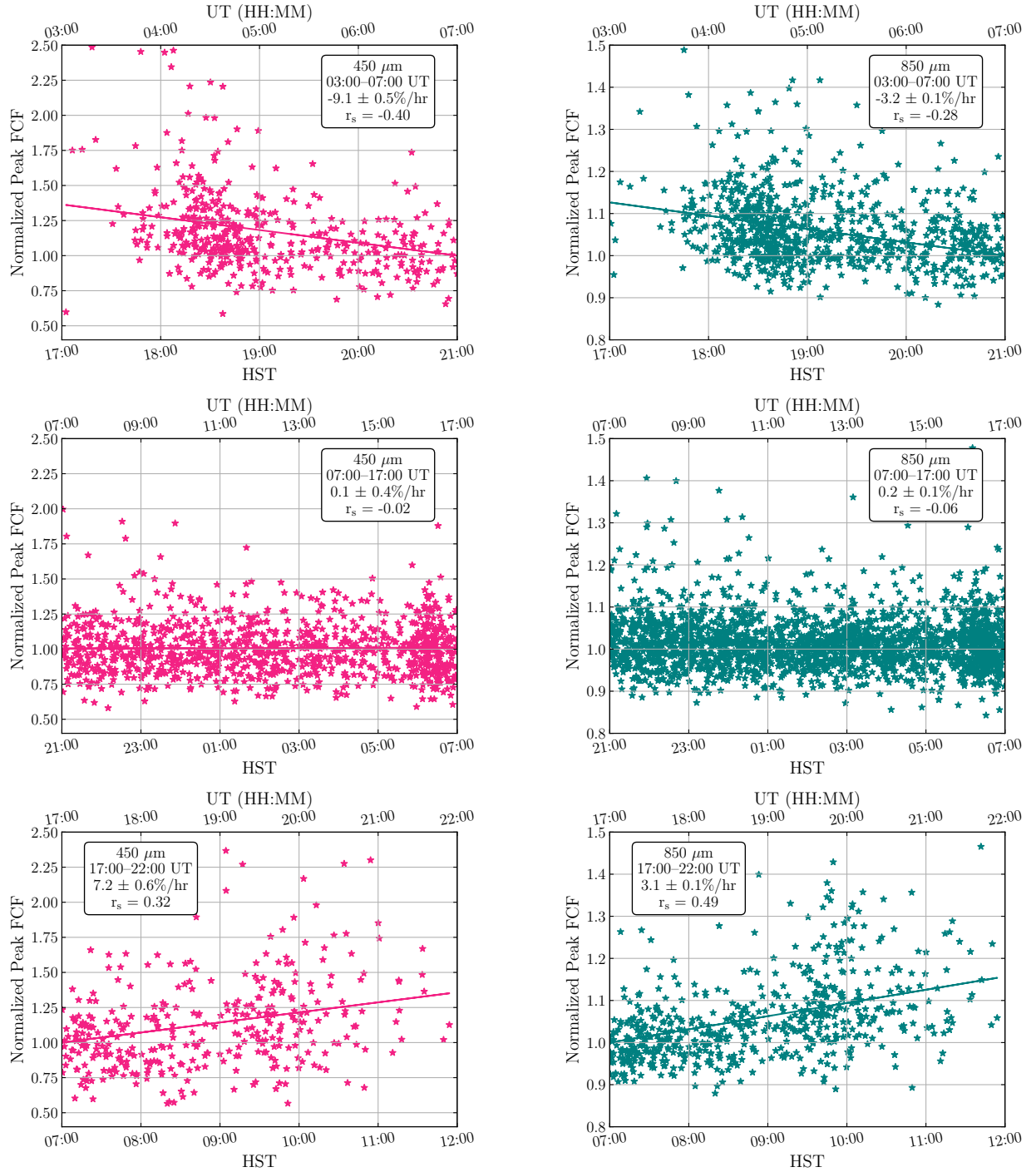


Figure 6. Normalized Peak FCFs at 450 (*left*) and 850 μm (*right*) derived using the primary calibrator Uranus and the secondary calibrator CRL 2688 as a function of observation time. Linear, bootstrapped least squares fits to the data and the associated Spearman Rank Correlation (r_s) are included in each panel. These results and their uncertainties are presented in Table 5 and can be used to modify the FCFs presented in Table 4 for observations taken outside of the stable time of night (0700–1700 UTC). *Top:* Evening observations (03:00–07:00 UTC). *Middle:* Stable observations (07:00–17:00 UTC). *Bottom:* Morning observations (17:00–22:00 UTC).

the beam profile becomes more stable and the flux more concentrated. During the night, 07:00 to 17:00 (UTC), the Peak FCFs remain stable. In the morning, after 17:00 (UTC), the dish expansion caused by the increasing temperature once again causes the beam profiles to degrade and the peak flux to decrease (Peak FCFs increase) at a rate of $7.2 \pm 0.6\% \text{ hr}^{-1}$ and $3.1 \pm 0.1\% \text{ hr}^{-1}$ at 450 and 850 μm , respectively. These results along with their associated Spearman Rank Correlation values (r_s) are summarised in Table 5. The Arcsecond FCFs do not vary significantly enough over the evening, night, or morning to warrant additional FCF correction factors during typical observing times.

5.1. Variations in the Beam

To illustrate the dish instability described in the previous section, an empirical measurement of the effective beam width (full width at half-maximum; FWHM_{eff}) can be made by comparing the derived Peak and Arcsecond FCFs (using the primary calibrator Uranus). In Equations 7 and 8, the flux of the source is measured in Jy beam^{-1} and Jy arcsec^{-2} , respectively. Therefore, dividing FCF_{peak} by $\text{FCF}_{\text{arcsec}}$ results in a measurement of the total beam area in arcsec^2 . Writing this in terms of the Gaussian FWHM introduces a factor of $\pi/[4 \ln(2)]$,

$$\text{FWHM}_{\text{eff}} \approx \sqrt{\frac{\text{FCF}_{\text{peak}}/\text{FCF}_{\text{arcsec}}}{\pi/[4 \ln(2)]}} \quad (9)$$

We find no significant difference when comparing the effective beam widths derived using Equation 9 before and after the SMU maintenance of 2018 June 30 (see Sections 4.1 and 4.1.1). Additionally, there is no significant trend with atmospheric transmission. In the top panels of Figure 7, we present the empirical FWHM_{eff} of the beam at 450 and 850 μm (left and right panels, respectively) as a function of time. The ‘‘U-shape’’ is directly related to the Peak FCF trends shown in the top panels of Figure 5. As discussed previously, the total-flux measurements are consistent over the course of the night while the peak-flux measurements undergo significant changes in the early evening and late morning. This suggests that flux from the primary beam component is diluted into the wings of the profile while staying within the $1'$ diameter aperture that was used to measure the total flux. The 450 μm effective beam FWHM during the stable part of the night (07:00–17:00 UTC) is $\sim 10.0 \pm 0.6''$. At 850 microns, the effective beam FWHM during the stable part of the night is $\sim 14.4 \pm 0.3''$, in good agreement with the values of $9.6''$ and $14.1''$ derived by D13.

In order to better separate secondary effects such as dish imperfections and distortions from the main lobe

response of the JCMT beam, we model both the 450 and 850 μm beam patterns as a combination of two Gaussian functions (D13):

$$G_{\text{total}} = \alpha G_{\text{MB}} + \beta G_{\text{S}}, \quad (10)$$

where each Gaussian profile, G , is of the form $\exp[-4 \ln(2) \times (r/\theta)^2]$, where r is the radial distance from the centre and θ is the FWHM of the profile, both measured in units of arcseconds. The first component, G_{MB} represents the ‘‘main beam’’ response. The second component, G_{S} , is an approximation of the ‘‘error beam’’, which describes the flux in the shoulders of the profile. α and β are coefficients describing the relative contribution of each component (the amplitudes). The broad error beam includes factors such as sidelobes due to diffraction, static dish deformations, and dish deformations induced by thermal gradients. Though this component is asymmetric, a Gaussian approximation allows for a simple measurement of its approximate volume. Combining the integrals of each profile provides the total beam volume, V ,

$$V = \frac{\pi}{4 \ln(2)} [\alpha(\theta_{\text{MB}})^2 + \beta(\theta_{\text{S}})^2] \text{ arcseconds}^2, \quad (11)$$

where θ_{MB} and θ_{S} represent the FWHM of the main beam and secondary (error) beam, respectively. The beam FWHMs were deconvolved by subtracting in quadrature the known size of Uranus at the time of the observation.

All observations of Uranus that were obtained when the atmospheric transmission was greater than 10% at 450 μm and 25% at 850 μm since 2011 May 1 were mapped in Az-El coordinates and modeled using Equation 10. The peak position and elongation angle of the planet were derived using Starlink’s (Berry et al. 2007) implementation of the GAUSSCLUMPS source-extraction algorithm (Stutzki & Guesten 1990). A slice through the peak position was then defined along the long axis of the beam profile and the position-flux information was extracted. The derived FWHM values for both the main- and error-beam components are statistically constant over both date and observing time. In contrast, the relative integrated volume of the error beam at each wavelength (Equation 11) varied as shown in the bottom panels of Figure 7 (450 and 850 μm on the left and right, respectively). This figure reveals a downward trend in the relative importance of the error beam (β) in the overall profile in the early evening and an upward trend in the late morning, mimicking the trend seen for the empirically measured effective FWHM (top panels). An error beam with a larger volume indicates that flux from the central region of the beam is being diluted into the

Table 5. Modifications to FCFs presented in Table 4 for observation times outside 07:00-17:00 (UTC).

Wavelength	Time Range (UTC)	FCF _{peak} ^a	Correction ^b (% hr ⁻¹)	Spearman Rank Correlation (r _s)
450 μm	03:00–07:00		9.1 ± 0.5	-0.40
450 μm	17:00–22:00		7.2 ± 0.6	0.32
850 μm	03:00–07:00		3.2 ± 0.1	-0.28
850 μm	17:00–22:00		3.1 ± 0.1	0.49

NOTE—^aArcsecond FCFs do not require an evening or morning modification to the stable FCFs presented in Table 4 but the uncertainty in the FCFs increase slightly during these times (see text).

^bIn the evening the Peak FCFs presented in Table 4 must be increased by the factor shown multiplied by the number of hours until 07:00 UTC. In the morning, the Peak FCFs presented in Table 4 must be increased by the factor shown multiplied by the number of hours since 17:00 UTC. Data obtained during the stable part of the night does not require a modification.

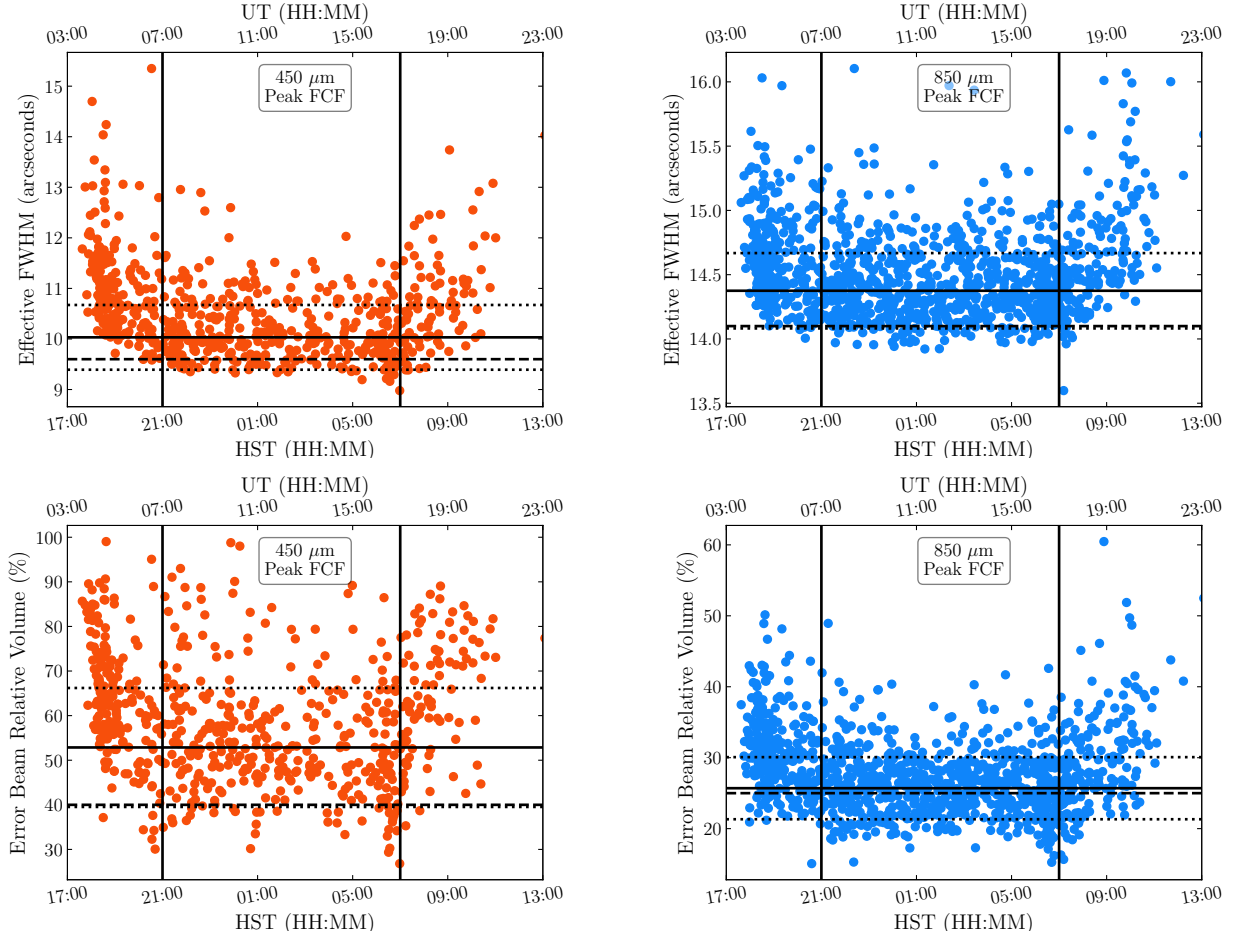


Figure 7. The empirical measurements of the effective beam FWHM derived using Equation 9 (*top*) and the relative volume of the error beam derived by the the two-component fit (Equation 10) (*bottom*) at 450 (*left*) and 850 μm (*right*) as a function of observation time. The primary calibrator Uranus was used to derive the FCFs in the top panels and the model fits in the bottom panels. The vertical lines mark the beginning and end of the stable observation period from 07:00–17:00 (UTC). The horizontal (dotted) lines show the standard deviation in the data for the stable observation period, centered on the median value over the stable observation period (horizontal, solid lines). The dashed, horizontal lines represent the original values derived by D13. The expansion and contraction of the dish during cooling and heating affects the beam size and, subsequently, the Peak FCFs.

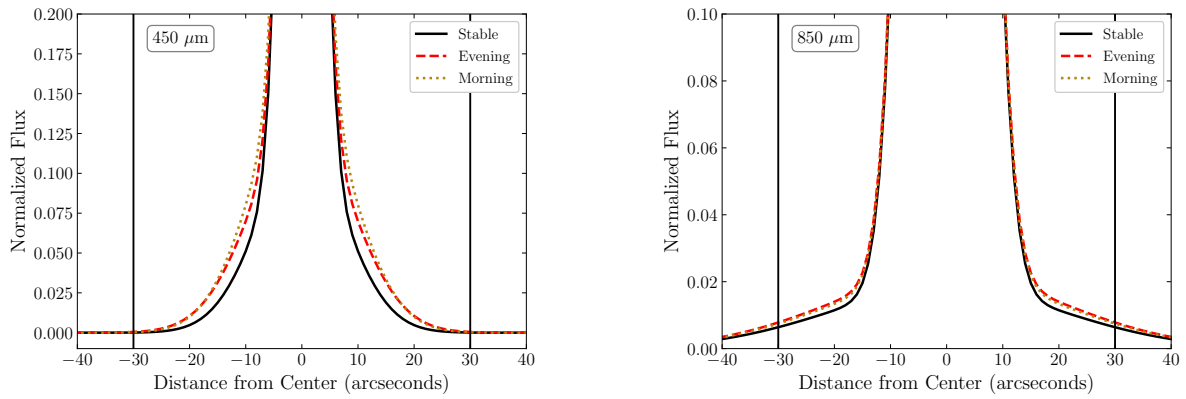


Figure 8. The two-component Gaussian beam model described in Equation 10 plotted at three different times: Evening (before 04:00 UTC; red, dashed line), Stable period of the night (07:00-17:00, UTC; black, solid line), and Morning (after 17:00 UTC; dotted, gold line) at 450 (*left*) and 850 μm (*right*). Throughout the course of the evening, stable, and morning intervals of a typical observing run, the main-beam component remains largely unchanged while the “wings” of the Gaussian flare during the evening and the morning as the secondary-beam (error) component is affected by changes in the dish shape as it heats and cools.

Table 6. Two-Component Gaussian Model Parameters (Equation 10)

	450 μm	850 μm
θ_{MB}^a (arcsec)	6.2 ± 1.0	11.0 ± 1.6
θ_{S}^b (arcsec)	18.8 ± 5.7	49.1 ± 8.4
α	0.89 ± 0.08	0.98 ± 0.01
β	0.11 ± 0.08	0.02 ± 0.01
Rel. vol. Main Beam	0.47 ± 0.12	0.74 ± 0.04
Rel. vol. Error Beam	0.53 ± 0.12	0.26 ± 0.04

NOTE—^aThe FWHM of the Main Beam component.

^bThe FWHM of the Error Beam component.

broad shoulders of the profile. During the stable portion of the night, the relative volumes of the error beams are $53\% \pm 12\%$ and $26\% \pm 4\%$ at 450 and 850 μm , respectively. The 850 μm value compares favorably with the previously derived 25% by D13, while the 450 μm value suggests the relative volume of the error beam is larger than the previously estimated 40%.

To illustrate the flux dilution in the early evening and late morning, Figure 8 shows the summed beam components, taking the median of the parameters α , β , θ_{MB} , and θ_{S} (Equation 10) in the evening, the stable period of the night, and the morning. The profile shoulders increase significantly during the unstable periods when the dish is cooling and heating with the setting and rising of the Sun. According to this symmetric model, at 450 μm there is approximately 10% more flux in the shoulders in the evening and morning than during the stable period of the night (8% in the evening and 12% in the morning). At 850 μm , the beam is much more stable; it has 2% more flux in the shoulders in the evening and morning when compared with the stable period of the night. These results suggest a slower degradation of the peak flux than seen in Figure 6, but that is a consequence of the assumed symmetry in the idealised model. As in the case of the empirically measured effective FWHM, there is no significant trend with atmospheric transmission.

The *expected* effective FWHM can be obtained by adding the two FWHM values calculated for each beam component in quadrature along with their respective weights,

$$\theta_{\text{eff},2\text{-comp}} = \sqrt{\alpha\theta_{\text{MB}}^2 + \beta\theta_{\text{S}}^2} \quad (12)$$

Using the median values for α , β , θ_{MB} and θ_{S} across the stable period of the night (see Table 6), we calculate an effective FWHM derived by the two-component fit of $\theta_{\text{eff},2\text{-comp}} = 8.6 \pm 1.3''$, for 450 μm and $12.6 \pm 1.9''$ for

850 μm . These are consistent with, though lower than the values of 9.8 and 14.6'' derived by D13.

6. SECONDARY-CALIBRATOR FLUXES

Since D13 presented the first on-sky calibration results, several of the secondary calibrators addressed in that work have been found to vary or be otherwise unreliable. In the present era, only four flux calibrator sources are routinely observed: CRL 2688, CRL 618, Arp 220, and HL Tau (in order of most to least frequent). Extinction-corrected peak and total-flux measurements were obtained of these most commonly used secondary calibrator sources (in units of pW) throughout the stable part of the night (07:00–17:00 UTC). Then, by applying the FCFs presented in Table 4 over the full 10-year datasets, updated 450 and 850 μm peak and total fluxes of these sources were derived in units of Jy. The results are presented in Table 7 and full light curves (including evening and morning observations) are presented in Appendix B. The same analysis was applied using the original extinction correction and FCF results derived by D13 on the full datasets and it was found that the updated values presented in this work reduced the scatter by 1–4% in the 450 μm light curves and 0.5–2% in the 850 μm light curves. This is due to the improved opacity relation and the approximately order of magnitude more observations used in each case. Figure 9 shows the four secondary calibrators in the context of previous flux measurements drawn from the literature, separating measurements that were made by fitting the peak of the source from those measurements that were made by aperture photometry. Some fluxes derived at wavelengths near to the 450 and 850 μm windows of interest are included such as: 500 μm observed by the Balloon-borne Large Aperture Submillimeter Telescope (BLAST), 800 μm observed by the now-retired UKT14 instrument of the JCMT, 860 μm observed by The Submillimeter Array (SMA), and 870 μm observed by the Atacama Pathfinder Experiment Telescope (APEX). See the figure caption for all literature references⁹. Below, each secondary calibrator is discussed in more detail.

6.1. CRL 2688

CRL 2688 (also known as the Egg Nebula; Ney et al. 1975) is a protoplanetary nebula located in the constellation of Cygnus at a distance of 920 pc. Its

⁹ None of the four secondary calibrators presented in this work are consistently observed with ALMA and when dust continuum flux measurements are performed, it is over a much smaller area of the source, focusing on substructures that are unresolved with single-dish telescopes.

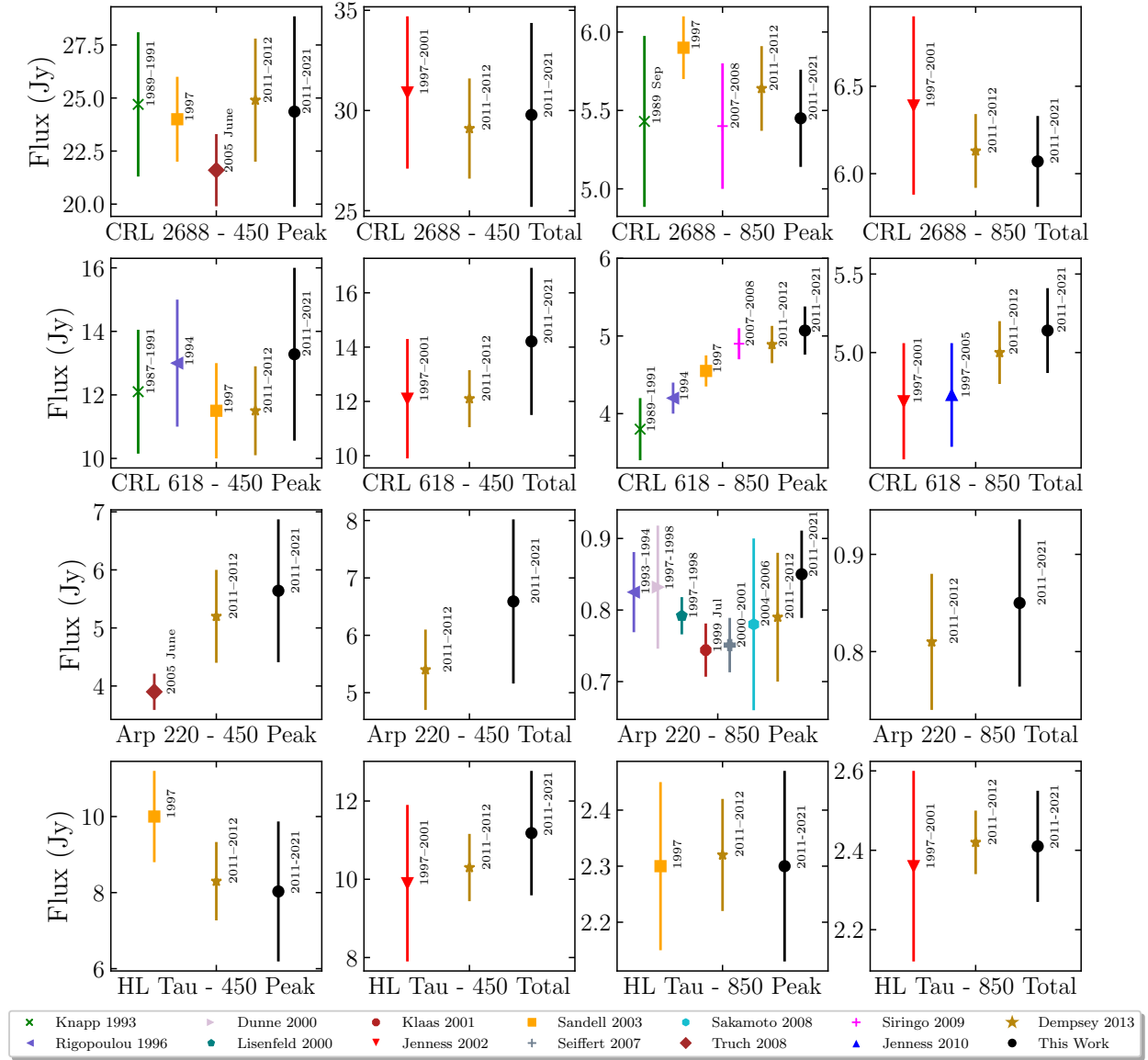


Figure 9. Secondary-calibrator fluxes compared in the literature. From top to bottom: CRL 2688, CRL 618, Arp 220, and HL Tau. From left to right: 450–500 μm peak flux, 450 μm total flux, 800–870 μm peak flux, and 850 μm total flux. Reported peak flux measurements were derived by fitting the source, whereas total-flux measurements were derived using aperture photometry. Green exes are the median values of the fluxes presented in Table 9 of Knapp et al. (1993) (JCMT, UKT14). Left-facing triangles are from Rigopoulou et al. (1996) (JCMT, UKT14, 800 μm). Right-facing triangles are from Dunne et al. (2000) (JCMT, SCUBA). Green pentagons are from Lisenfeld et al. (2000) (JCMT, SCUBA). Red octagons are from Klaas et al. (2001) (JCMT, SCUBA). Downward-facing triangles are from Jenness et al. (2002) (JCMT, SCUBA). Orange squares are from Sandell (2003) (JCMT, SCUBA). Gray crosses are from Seiffert et al. (2007) (JCMT, SCUPOL). Cyan hexagons are from Sakamoto et al. (2008) (SMA, 860 μm). Brown diamonds are from Truch et al. (2008) (BLAST, 500 μm). Magenta crosses are from Siringo et al. (2009) (APEX, LABOCA 870 μm). Blue upward-facing triangles are from Jenness et al. (2010) (JCMT, SCUBA). Light brown stars are from D13 (JCMT, SCUBA-2). Black circles are from this work (JCMT, SCUBA-2).

Table 7. Secondary-calibrator Fluxes.

Source	R.A. (J2000)	Dec. (J2000)	450 μm Peak (Jy beam $^{-1}$)	850 μm Peak (Jy beam $^{-1}$)	450 μm Total (Jy)	850 μm Total (Jy)	Num. 450	Num. 850
CRL 2688	21:02:18.27	36:41:37.00	24.36 ± 4.49	5.45 ± 0.31	29.78 ± 4.59	6.07 ± 0.26	691	1482
CRL 618	04:42:53.67	36:06:53.17	13.28 ± 2.72	5.07 ± 0.31	14.21 ± 2.71	5.14 ± 0.27	608	1237
Arp 220	15:34:57.27	23:30:10.48	5.64 ± 1.23	0.85 ± 0.06	6.59 ± 1.43	0.85 ± 0.09	322	501
HL Tau	04:31:38.44	18:13:57.65	8.03 ± 1.84	2.30 ± 0.17	11.18 ± 1.59	2.41 ± 0.14	34	37

NOTE—Secondary-calibrator fluxes derived by applying the FCFs presented in Table 4 to the extinction-corrected raw flux measurements obtained during the stable part of the night. The number of 450 μm observations used is less than its 850 μm counterpart due to the exclusion of low-transmission data, which could not be used to fit a reliable peak flux. Secondary-calibrator light curves including all data from evening, stable, and morning observations are presented in Appendix B.

significant, consistent thermal dust emission that is bright at submillimetre wavelengths qualify the source to be a robust standard calibrator. The new FCFs derived in this work reduce the uncertainty in the 450 μm peak and total flux by 2% and 4%, respectively, when compared with data corrected by the original extinction correction and FCFs derived in D13. The 850 μm peak and total-flux uncertainties are reduced by 0.5% and 1%, respectively. For CRL 2688, we derive median peak-flux values of 24.36 ± 4.49 Jy beam $^{-1}$ and 5.45 ± 0.31 Jy beam $^{-1}$ and total-flux values of 29.78 ± 4.59 Jy and 6.07 ± 0.26 Jy at 450 and 850 μm , respectively. The measured fluxes derived in this work are consistent with previous values noted in the literature (see Figure 9). The 850 μm peak flux obtained in 1997 (Sandell 2003) appears to be anomalously high. While there is no direct ~ 850 μm measurement during the 2005 BLAST mission (Truch et al. 2008), the 850 μm flux derived by the spectral energy distribution (SED) fit is also consistent with the most-recent SCUBA-2 measurements. Compared with D13, both the 450 and the 850 μm peak and total-flux values agree to within 3% with the original work. This source does not appear to vary significantly over time.

6.2. CRL 618

CRL 618 (also known as the Westbrook Nebula; Westbrook et al. 1975) is another strong source of thermal dust emission: a bipolar reflection nebula illuminated by a central B0 star and located in the constellation of Auriga at a distance of 920 pc. The new FCFs derived in this work reduce the uncertainty in the 450 μm peak and total flux by 1% and 2%, respectively, when compared with the original extinction correction and FCFs derived in D13. The 850 μm peak and total-flux uncertainties are both reduced by 2%. For CRL 618, we derive median peak-flux values of 13.28 ± 2.72 Jy beam $^{-1}$ and 5.07 ± 0.31 Jy beam $^{-1}$ and total-flux values of 14.21 ± 2.71 Jy and 5.14 ± 0.27 Jy at 450 and 850 μm , respectively. Comparing with D13, the 450 μm peak and total-flux values are 16% and 18% higher than those derived in the previous work, while the 850 μm peak and total-flux values are within 4%. While Jenness et al. (2002, 2010) report no variability in the 850 μm flux of CRL 618 throughout 1997–2005 (using aperture photometry to measure the total flux), there is an indication that the source is now significantly brighter than it was between 1989–1994. Knapp et al. (1993) report 1.3 and 1.1 mm data that tentatively show a steady increase with time, while their 450 and 800 μm data showed no increase to within the measured uncertainties. The authors note that the 450 μm emission is likely to be

dominated by warm dust, while longer (near-millimeter wavelengths) are dominated by emission from the small central HII region. We present 10-year light curves between 2011–2021 in Appendix B. These show no significant overall changes in either peak or total flux during this time period at 450 μm ; no significant changes in the total flux at 850 μm ; and a slight, but discernible, upward trend in the peak flux at 850 μm . The linear increase in 850 mum over this 10-year period appears to be at the rate of 0.036 ± 0.003 Jy/yr. A simple comparison between the most-recent flux measurement of 5.2 Jy derived in this work to the flux of 3.8 Jy derived in 1991 by Knapp et al. (1993) suggests an average increase of ~ 0.046 Jy/yr, implying that the brightening of CRL 618 at 850 μm may have been approximately steady over a 30-year period. It is recommended that CRL 618 is used as a calibrator with caution, ensuring that flux measurements on a given night are compared with data obtained over at least the previous several months.

6.3. Arp 220

Arp 220 (Soifer et al. 1984; Neugebauer et al. 1984) is the closest ultra-luminous infrared galaxy (ULIRG) and the most-luminous object in the local universe. The new FCFs derived in this work reduce the uncertainty in the 450 μm peak and total flux by 2% and 3%, respectively, when compared to the original extinction correction and FCFs derived in D13. The 850 μm uncertainties are the same. For Arp 220, we derive median peak-flux values of 5.64 ± 1.23 Jy and 0.85 ± 0.06 and total-flux values of 6.59 ± 1.43 Jy and 0.85 ± 0.09 Jy at 450 and 850 μm , respectively. At 850 μm , the measured peak and total flux of the source are statistically indistinguishable. As discussed in Section 4, a true point source has an equivalent value in units of Jy beam $^{-1}$ and Jy. Comparing with D13, the 450 μm peak and total-flux values are 9% and 23% higher than those derived in the previous work, while the 850 μm peak and total-flux values are 5% and 8% higher. These new flux results are otherwise broadly consistent with previous measurements in the literature with some evidence of the source dimming, then brightening at 850 μm over the past ~ 30 years. The 500 μm BLAST data (Truch et al. 2008) indicates a low flux in 2005 relative to the 2011–2021 measurements, while the predicted 850 μm flux extrapolated from the SED fit is consistent with the flux measured by Sakamoto et al. (2008) with the SMA during the same time period. The 10-year light curves presented in Appendix B may indicate a slight downward trend in flux since 2012.

6.4. HL Tau

HL Tau (Landolt 1968) is a young T Tauri star still associated with its nascent dust and gas located at a distance of 140 pc towards the Taurus constellation. T Tauri stars are variable by nature, so this is the least frequently used flux calibrator source for SCUBA-2 observations. Only ~ 30 observations have been performed during the stable part of the night over the course of 10 years (~ 60 in total). The new FCFs derived in this work reduce the uncertainty in both the 450 μm peak and total flux by 4% when compared with the original extinction correction and FCFs derived in D13 while the 850 μm peak and total-flux uncertainties are approximately the same. For HL Tau, we derive median peak-flux values of $8.03 \pm 1.84 \text{ Jy beam}^{-1}$ and $2.30 \pm 0.17 \text{ Jy beam}^{-1}$ and total-flux values of $11.18 \pm 1.59 \text{ Jy}$ and $2.41 \pm 0.14 \text{ Jy}$ at 450 and 850 μm , respectively. Comparing with D13, the 450 μm peak-flux value is within 3%, but the total-flux value is 10% higher than those derived in the previous work (this is still consistent to within the uncertainty). The 850 μm peak and total-flux values are within 1%. 450 μm peak flux measured in 1997 (Sandell 2003) appears significantly brighter than recent flux measurements. The total 450 μm flux and both 850 μm fluxes are consistent with the other measurements from the literature. Note that HL Tau was measured to have a significantly lower peak flux at both wavelengths in 2014 June/July (see Appendix B).

7. CASE STUDY: QUASAR 3C 84

Quasars are common bandpass calibrator sources for interferometers due to their high brightness and small angular size. While quasars are not used at the JCMT as standard flux calibrators due to their variable nature, they are used throughout the night to calibrate the pointing model¹⁰. Figure 10 shows 10 years of pointing-correction observations toward Quasar 3C84 using the JCMT (blue stars), along with calibration observations for the SMA (red squares), and ALMA (gold triangles). The SMA data were obtained using the ‘‘Submillimeter Array Calibrator List’’ website¹¹ and the ALMA data were obtained via the ‘‘ALMA Calibrator Catalogue’’¹². The raw JCMT data has been post-processed by applying the new extinction correction presented in Equation 6 (using the values given in Table 1) and the rec-

ommended FCFs presented in Table 4 (along with the modifications in Table 5). In the left panel, the Peak FCFs were used and the resulting peak fluxes were measured with a 2D Gaussian function using CUPID’s GAUSS-CLUMPS program (Berry et al. 2013; Stutzki & Guesten 1990). Background subtraction is treated as a free parameter in the fit. In the right panel, the Arcsecond FCFs were used and the total fluxes were measured using a 60’’-diameter aperture employing a background subtraction where the background level was measured in an annulus with inner and outer diameters of 90 and 120’’.

The JCMT data calibrated in both ways is self consistent (the peak flux and total flux should be equal for a true point source) and broadly consistent with the interferometric data. The SMA data appear to consistently return higher fluxes than the ALMA data while the JCMT data agrees better with the ALMA data and in some cases reports lower fluxes. Applying the previous recommended extinction correction and FCFs presented by D13 across the full light curve results in the JCMT data better agreeing with the SMA data, often reporting values higher than those measured at ALMA. The 2D Gaussian fit used to measure the flux for the left panel of Figure 10 is subject to higher uncertainty, especially in poor weather when the flux concentration is diluted from the main beam into the wings of the profile. In this case, the 2D Gaussian fit to the peak will underestimate the true flux. Anomalously low flux measurements are the result of focus issues. While the aperture photometry used to produce the measurements in the right panel of Figure 10 is more robust to variations in the beam, the background subtraction can add uncertainty if there are issues producing a smooth, uniform map background as a result of uncertainties in the data reduction.

These results indicate that it is not only the applied extinction correction and FCFs for a given data set that fully determine the uncertainty in the measurement; the flux determination method also contributes to the scatter. Assuming a robust background subtraction can be performed, the aperture photometry method mitigates the affect of beam dilution due to poor weather or temperature gradients across the dish and is, overall, preferred over peak fitting.

8. SUMMARY

Since SCUBA-2’s commissioning phase ended a decade ago, thousands of observations of calibrator sources have been obtained in a wide range of weather conditions, spanning the evening through the late morning. D13 derived the initial atmospheric extinction cor-

¹⁰ Structural imperfections of the telescope result in small offsets from the commanded slew position. Bright sources with known positions are observed frequently to update the pointing model, yielding a reasonable accuracy of $\sim < 3''$.

¹¹ <http://sma1.sma.hawaii.edu/callist/callist.html>

¹² <https://almascience.eso.org/alma-data/calibrator-catalogue>

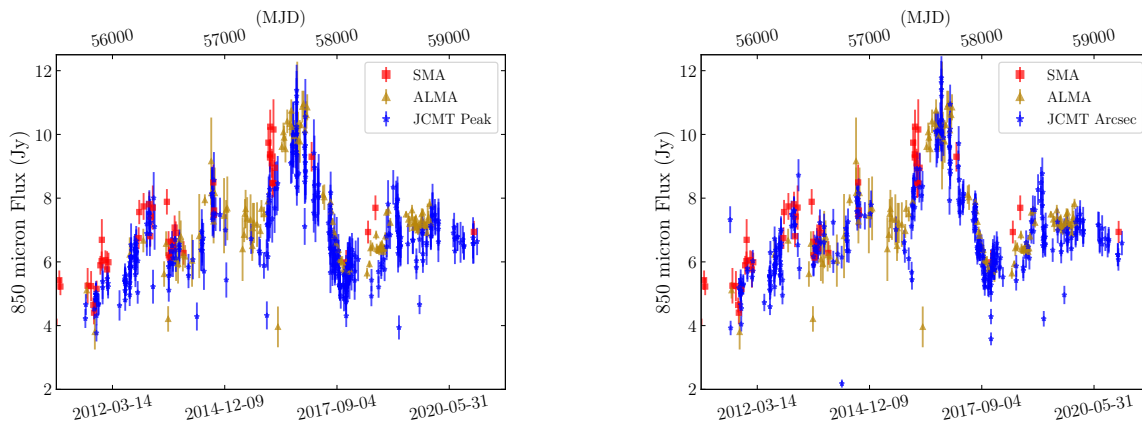


Figure 10. The 850 μm flux of Quasar 3C84 plotted over 10 years. Data obtained by the Submillimeter Array (SMA; red squares), the Atacama Large Millimeter/Submillimeter Array (ALMA; gold triangles), and the JCMT (blue stars) are included in each panel. The JCMT calibration employs the results presented in Table 4 with the modifications presented in Table 5. *Left:* JCMT flux measured using a Gaussian fit to the data. Peak FCFs are applied. *Right:* JCMT flux is derived using aperture photometry with a 60 arcsecond diameter aperture and background subtraction calculated over a 90–120 arcsecond (inner, outer) diameter annulus. Arcsecond FCFs are applied. The JCMT flux measurements in each panel are in agreement with one another and largely in agreement with the SMA and ALMA observations.

rection and FCFs based on one year of data between 2011–2012. Since that time, the telescope has undergone hardware updates and changes that have impacted the calibration at both 450 and 850 μm . Below is a summary of the updated recommendations for calibrating both archival and new SCUBA-2 data obtained by the JCMT:

1. A new opacity relation to be used in the atmospheric extinction correction was derived by minimising the variance in the corrected flux of the primary calibrator, Uranus, and secondary calibrators, CRL 2688 and CRL 618 as a function of atmospheric transmission. The form of the non-linear relation is presented in Equation 6 with the best-fit parameters presented in Table 1. The correction is performed by substituting the opacity relation into Equation 1 (see Section 3 for details).
2. After the new extinction correction is applied to the raw data, the flux is calibrated by applying the (multiplicative) Peak and Arcsecond FCF values presented in Table 4 (see Section 4 for details). The FCFs vary as a function of date, accounting for: a) the upgrade of the thermal-filter stack in 2016 November, which improved transmission at 850 μm and b) the SMU maintenance in 2018 May/June, which improved the flux concentration and lowered the FCF values at both wavelengths (see Section 4.1.1).
3. For data observed outside the hours of 07:00–17:00 UTC, temperature gradients across

the dish due to the setting and rising of the sun necessitate corrections to the Peak FCFs to account for beam degradation (wherein flux from the main-beam component is diluted into the wings of the approximately Gaussian beam profiles). These linear corrections as a function of time of night are presented in Table 5 (see Section 5 for details). The effective beam widths and relative volumes of the main and error (secondary) beam are presented in detail as a function of time in Section 5.1. Results of the two-component beam models can be found in Table 6.

The updated opacity relations and stable time-of-night FCFs presented in this work (first two points) are now the default used in the STARLINK data reduction and calibration software as of the software’s 21A release¹³. If desired, the FCF corrections for data observed before 07:00 UTC or after 17:00 UTC (during the evening and morning) must be applied manually¹⁴. Between 07:00 and 17:00 UTC, the portion of the night that is most stable to temperature gradients that cause dish deformation, the total and peak calibrator flux uncertainties measured at 450 μm are found to be 14% and 17%, respectively. Measured at 850 μm , the uncertainties are 6%, and 7%. During the evening (pre 07:00 UTC) and morning (post 17:00 UTC), the increased

¹³ <https://starlink.eao.hawaii.edu>

¹⁴ Detailed information can be found on the East Asian Observatory tutorial page: <https://www.eaoobservatory.org/jcmt/science/reductionanalysis-tutorials/>

scatter and uncertainty in the linear-fit corrections of the Peak FCF values result in a few percent increase in the relative calibration errors presented in Table 4.

In Section 6, we applied the new extinction correction and FCFs to the four most commonly used secondary calibrators: CRL 2688, CRL 618, Arp 220, and HL Tau to derive updated flux estimates and to investigate long-term changes in calibrator brightnesses. While CRL 2688 and HL Tau are consistent with previous measurements derived in the literature and show no discernible variability over time, CRL 618 and Arp 220 present less reliable light curves and require significant updates to the results presented by D13 (see Figure 9). 10-year light curves for all calibrator sources are presented in Appendix B, Table 8 (machine-readable tables are available in the online version).

The updated calibrations are also applied to 850 μm observations of Quasar 3C84 (a JCMT pointing offset calibrator) and compared with fluxes obtained by SMA and ALMA. The measured JCMT fluxes corrected by the Peak and Arcsecond FCFs are consistent with one another and are broadly consistent with the interferometric data. The method of flux determination contributes to the overall uncertainty of the measurement (see Section 7 for details).

Calibrator maps can be downloaded from the Canadian Astronomy Data Centre (CADC)¹⁵ by searching “Proposal ID: JCMTCAL”. Up-to-date information is posted on the JCMT SCUBA-2 calibration website: <https://www.eaobservatory.org/jcmt/instrumentation/continuum/scuba-2/calibration/>.

ACKNOWLEDGMENTS

The authors wish to recognise and acknowledge the very significant cultural role and reverence that the summit of Maunakea has always had within the indigenous Hawaiian community. We are most fortunate to have the opportunity to conduct observations from this mountain. The comments provided by the anonymous referee have significantly strengthened this work. The James Clerk Maxwell Telescope is operated by the East Asian Observatory on behalf of The National Astronomical Observatory of Japan; Academia Sinica Institute of Astronomy and Astrophysics; the Korea Astronomy and Space Science Institute; the Operation, Maintenance and Upgrading Fund for Astronomical Telescopes and Facility Instruments, budgeted from the Ministry of Finance (MOF) of China and administrated by the Chinese Academy of Sciences (CAS), as well as the National Key R&D Program of China (No. 2017YFA0402700). Additional funding support is provided by the Science and Technology Facilities Council of the United Kingdom and participating universities in the United Kingdom and Canada. Additional funds for the construction of SCUBA-2 were provided by the Canada Foundation for Innovation. This research used the facilities of the Canadian Astronomy Data Centre operated by the National Research Council of Canada with the support of the Canadian Space Agency. The James Clerk Maxwell Telescope has historically been operated by the Joint Astronomy Centre on behalf of the Science and Technology Facilities Council of the United Kingdom, the National Research Council of Canada and the Netherlands Organisation for Scientific Research. The Starlink software (Currie et al. 2014) is currently supported by the East Asian Observatory.

Facilities: JCMT

Software: astropy (Astropy Collaboration et al. 2013), matplotlib (Hunter 2007), aplpy (Robitaille & Bressert 2012), Starlink (Currie et al. 2014),

APPENDIX

A. FLUX UNCERTAINTY

While a full analysis of the myriad contributions to flux uncertainty is beyond the scope of this paper, here we provide a broad discussion of the more notable is-

sues. There is seemingly no obvious parameter that is the singular dominant cause of the inherent scatter in the calibrator light curves. Before the light is received by the detector, the effect of the bright and variable atmosphere at submillimeter wavelengths is removed by an approximation that assumes an atmospheric model that is plane-parallel. The true atmosphere may not be

¹⁵ <https://www.cadc-ccda.hia-ihp.nrc-cnrc.gc.ca/>

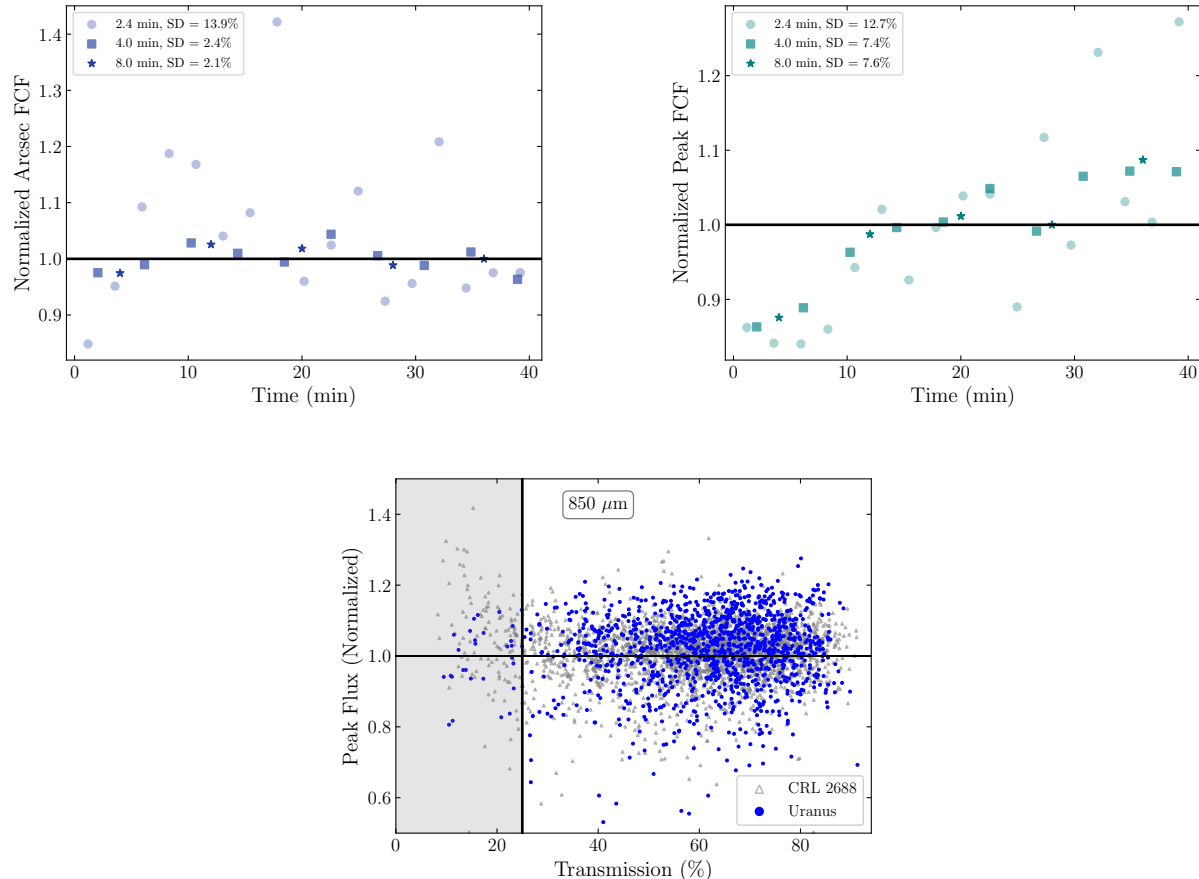


Figure 11. *Top:* Normalized Arcsecond (*left*) and Peak (*right*) FCFs derived for ~ 2.4 minute (circles), 4 minute (squares), and 8 minute (stars) subsections of the raw data for a single, 40 minute, $850\ \mu\text{m}$ observation of CRL 2688. The data were taken with $\tau_{225} \sim 0.3$ and Airmass ranging between 1.18 – 1.31. Solid, horizontal lines are shown at a value of 1.0 to represent the normalized median FCF values. *Bottom:* The normalised $850\ \mu\text{m}$ peak fluxes of Uranus (blue circles) and CRL 2688 (gray triangles) as a function of atmospheric transmission. The peak-flux response of the primary calibrator Uranus is flat across the full transmission range whereas the peak flux of CRL 2688 is over-corrected below a transmission of 25%.

well described by this model and low-lying variations in weather conditions with scale heights comparable to several times the height of the JCMT facility complicate the matter further. In addition, the calibration of the water-vapor monitor brightness temperatures and the parabolic fit used to estimate the properties of the 183 GHz water line introduce uncertainties in the PWV measured for use in the extinction correction. Subtle atmospheric effects such as the submillimeter seeing, wind speed, ambient-temperature changes, and humidity will all contribute lower-level contributions to beam distortions and, subsequently, flux measurements. Measuring fluxes by fitting the peak of a compact source will be affected more than measurements performed using aperture photometry as each of the more subtle atmospheric effects works to dilute the main-beam flux.

The GORE-TEX™ membrane that protects the dish from the high-altitude elements is not 100% transmis-

sive at submillimeter wavelengths. During the commissioning of the POL-2 instrument, the membrane was removed in order to increase the sensitivity at $450\ \mu\text{m}$ and to better understand its affect on the instrumental polarisation (IP). The weather conditions that allow for the JCMT to observe while the membrane is removed are pristine and limited. A provisional analysis of calibrator observations observed during the membrane removal suggests a decrease in $850\ \mu\text{m}$ Peak FCF values by 6–7% and a decrease in $850\ \mu\text{m}$ Arcsecond FCF values by 4–5%. The uncertainty, however, is increased as the dish is exposed and unstable due to wind¹⁶. At $450\ \mu\text{m}$, the increase in flux uncertainty masked any improvement in sensitivity due to the removal of the membrane.

¹⁶ While the membrane is removed, the maximum wind speed during which the JCMT can operate is 18 mph.

Finally, instrumental noise, non-cooled optical components, and uncertainties in the MAKEMAP routine’s modeling and removal of noise components from the time stream (or introduction of map artifacts, see Chapin et al. 2013, for details) can all introduce uncertain contributions to the final flux.

None of these individual factors alone dominate the scatter. Therefore, quantifying each noise contribution is a difficult task that requires a significant amount of observations taken under controlled conditions. Even then, there are atmospheric conditions that cannot be measured. To assess the changes in FCFs taken throughout approximately stable conditions during a time of poor atmospheric transmission (where the FCFs have a larger scatter and tend to over-correct, see Figure 1), a single 40 minute long observation of CRL 2688 was performed. The observation took place on 2018 October 10 at 08:15 (UTC) (stable period of the night) in Weather Band 5, ($\tau_{225} = 0.3$). The setting source had an airmass that ranged from 1.18–1.31 over the course of the observation, yielding an atmospheric transmission range at $850 \mu\text{m}$ from 21–17%¹⁷.

This 40 minute observation was subdivided into 17 ~ 2.4 minute maps using MAKEMAP’s SHORTMAPS command and FCF values were derived for each sub-observation. A 2.4 minute integration time was chosen to match the typical individual calibrator observations taken in the wettest weather. The SHORTMAPS command first produces a “total” map using all data. Then, the map for each 2.4 minute period (each *shortmap*) is constructed by adding the total map onto a map made from the time-series residuals for each shortmap. In this way, each shortmap is made using the same final sky model (produced for the total map after noise subtraction; see Chapin et al. (2013) for details) and the increased noise in each shortmap is due only to the shorter amount of input time-series data. Using the same sky model for each observation reduces the scatter in the FCFs when compared to performing a series of individual observations (which will each produce a slightly different sky model based on the available data). The normalized $850 \mu\text{m}$ results are shown in the top panels of Figure 11 (circles).

The Arcsecond FCFs are consistent with a constant value over the 40 minute observation despite the increasing transmission as the source was setting. The Peak FCFs, however, show an obvious increasing trend as the transmission decreases. In the bottom panel of

Figure 11, the peak-flux response as a function of atmospheric transmission is shown for Uranus and CRL 2688 over all calibrator observations (compare with the right panel of Figure 1). Uranus’s peak flux is constant across all atmospheric transmissions whereas the peak flux of CRL 2688 is clearly over-corrected below a transmission of 25%. CRL 2688 is not a point source even at the JCMT’s resolution of $\sim 14.5''$ at $850 \mu\text{m}$, and it is the recovery of this extended structure in poor transmission, short integration time (i.e. high uncertainty) observations that causes an artificial depression in the peak flux while the total flux across the source remains conserved. Therefore, it is especially important to calibrate poor transmission maps of compact sources with the Arcsecond FCFs and perform aperture photometry to measure robust fluxes. An investigation of each shortmap, individually, revealed that the 2.4 minute typical integration time resulted in SNR values ranging from 2.8 – 5.1 (decreasing with time as the source was setting). Therefore, additional sets of shortmaps were produced that divided the ~ 40 minute observation into 4 and 8 minute sub-observations and the analysis was repeated (see squares and stars plotted in Figure 11). The increased integration times improved each flux measurement resulting in minimum SNR values of ~ 4.4 . There is no significant difference between the FCF distributions derived by the 4 and 8 minute shortmap datasets, so for efficiency, calibrator integration times are now increased to 4 minutes in the rare times that SCUBA-2 is used during very wet weather conditions in order to improve the flux estimates. The poor transmission during the observation resulted in an SNR that was insufficient to conduct the same analysis at $450 \mu\text{m}$.

B. SECONDARY-CALIBRATOR LIGHT CURVES

10-year light curves of the 450 and $850 \mu\text{m}$ peak and total fluxes of the four most commonly used secondary flux calibrators are presented in Figures 12 (Arp 220 and CRL 2688 at $450 \mu\text{m}$), 13 (Arp 220 and CRL 2688 at $850 \mu\text{m}$), 14 (CRL 618, and HL Tau at $450 \mu\text{m}$), and 15 (CRL 618, and HL Tau at $850 \mu\text{m}$). The solid lines represent the median value of the distribution and the dashed lines show the median absolute deviation added in quadrature to the 5% uncertainty in Uranus’ (the primary calibrator) flux model. Table 8 gives an example of the information that is provided for all these secondary-calibrator sources in machine-readable tables in the online version of the paper.

The 450 and $850 \mu\text{m}$ CRL 2688 light curves are consistent with constant flux values over time. The $450 \mu\text{m}$ Peak flux of Arp 220 perhaps shows an indication of a parabolic shape with lower flux values reported through-

¹⁷ Note that these observations were excluded from the analysis in the main paper as the atmospheric transmission did not pass the 25% threshold.

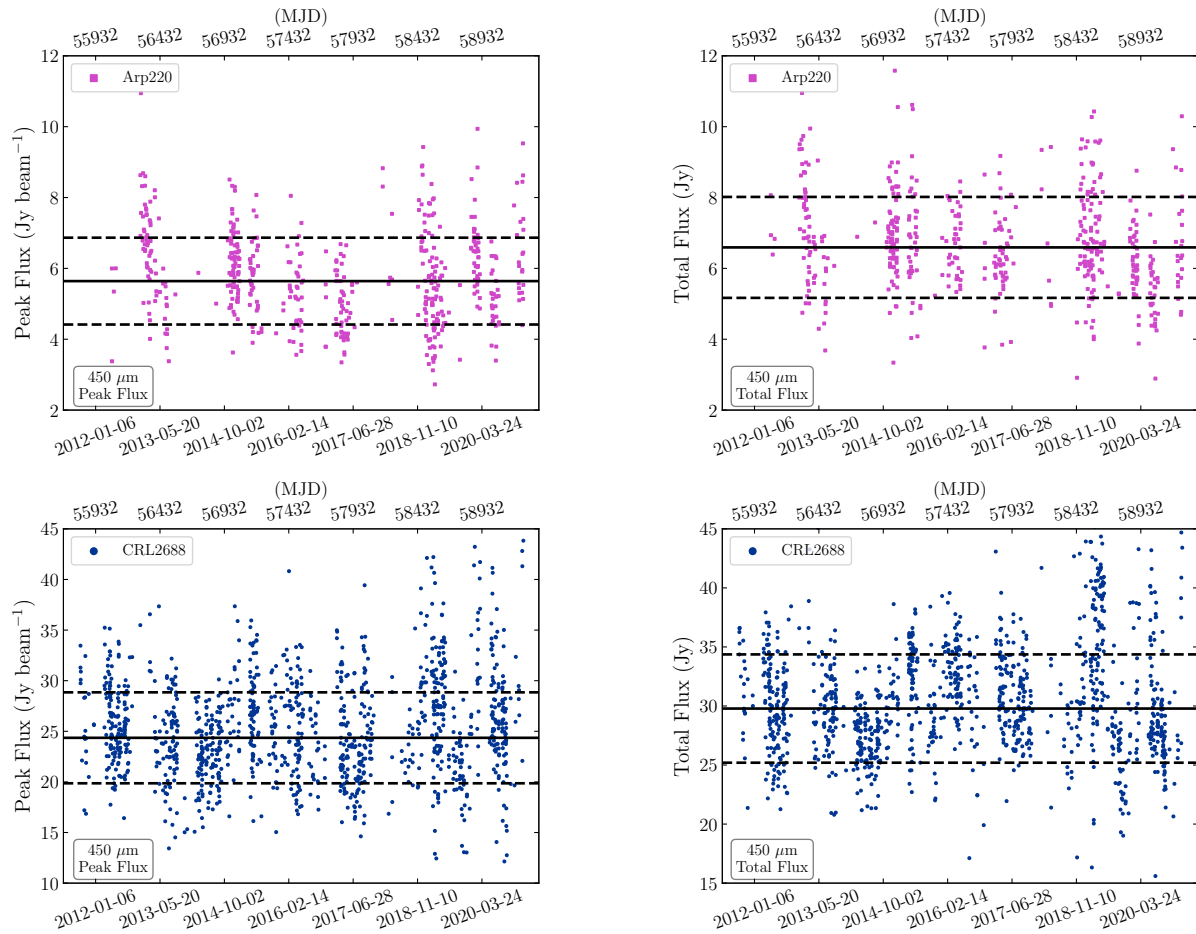


Figure 12. The peak (*left*) and total (*right*) fluxes derived for secondary-calibrator sources Arp 220 (*top*) and CRL 2688 (*bottom*) at $450\ \mu\text{m}$ using the FCFs presented in Table 4, along with the modifications presented in Table 5. The solid line represents the median value of the distribution and the dashed line shows the standard deviation of the light curve.

out 2016 and early 2017, but the $450\ \mu\text{m}$ total-flux light curve appears constant over time within the uncertainties. At $850\ \mu\text{m}$, however, the Arp 220 peak-flux values appear constant, whereas the total-flux values appear to decrease linearly at the rate of $0.009 \pm 0.002\ \text{Jy}/\text{year}$. The HL Tau peak and total fluxes at each wavelength also appear broadly constant over time with the exception of 2014, where fluxes appear anomalously low. The majority of these data were obtained in the months of June and July.

CRL 618 shows the most indications of variability when compared with the other secondary-calibrator sources. At $850\ \mu\text{m}$ the peak flux clearly increases over time. A simple linear fit to the data suggests a brightening at a rate of $0.036 \pm 0.003\ \text{Jy}/\text{yr}$. Therefore, over the course of 10 years, the peak flux has increased by

$0.36\ \text{Jy}$, or, $\sim 7\%$. There also appears to be a quasi-periodic trend of brightening and dimming on much shorter (\sim yearly) timescales than the overall secular increase. The total flux does not show the same linear, upward trend, reporting a roughly constant value equivalent to the brightest peak flux (measured in early 2021). In both the peak and total flux light curves, the data obtained between 2011–2012 appears to be at a lower value than the subsequent data obtained, highlighting the difference between the measured values in this paper and those in D13. At $450\ \mu\text{m}$, the larger scatter in the distribution masks any upward trend that may exist in the peak flux, though there are still indications of a quasi-periodic brightening and dimming, especially before 2017.

REFERENCES

Astropy Collaboration, Robitaille, T. P., Tollerud, E. J., et al. 2013, *A&A*, 558, A33

Berry, D. S., Reinhold, K., Jenness, T., & Economou, F. 2007, in *Astronomical Society of the Pacific Conference Series*, Vol. 376, *Astronomical Data Analysis Software and Systems XVI*, ed. R. A. Shaw, F. Hill, & D. J. Bell, 425

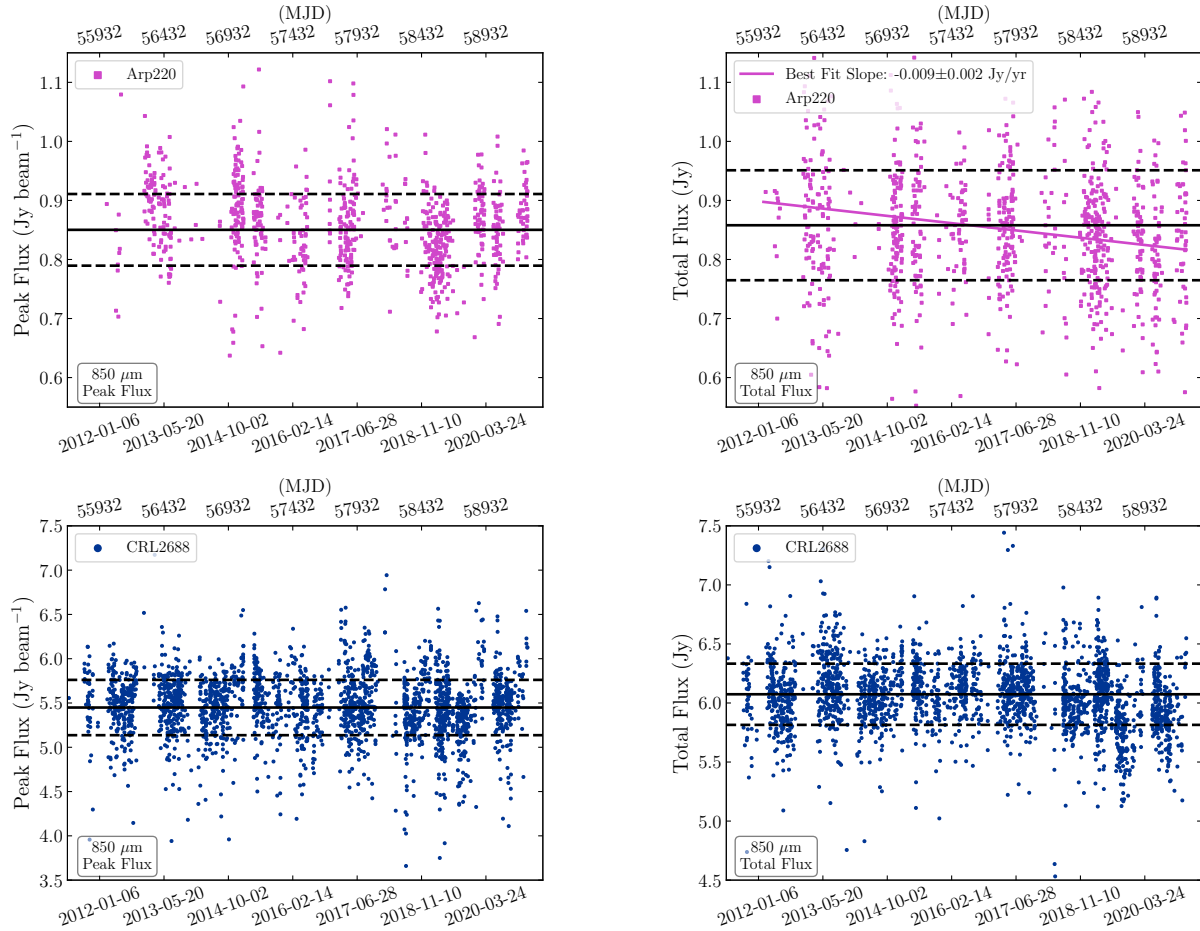


Figure 13. The peak (*left*) and total (*right*) fluxes derived for secondary-calibrator sources Arp 220 (*top*) and CRL 2688 (*bottom*) at $850\ \mu\text{m}$ using the FCFs presented in Table 4, along with the modifications presented in Table 5. The solid line represents the median value of the distribution and the dashed line shows the standard deviation of the light curve.

Berry, D. S., Reinhold, K., Jenness, T., & Economou, F.

2013, CUPID: Clump Identification and Analysis Package, ASCL, ascl:1311.007

Bintley, D., MacIntosh, M. J., Holland, W. S., et al. 2010, in Society of Photo-Optical Instrumentation Engineers (SPIE) Conference Series, Vol. 7741, Millimeter, Submillimeter, and Far-Infrared Detectors and Instrumentation for Astronomy V, ed. W. S. Holland & J. Zmuidzinas, 774106

Bintley, D., MacIntosh, M. J., Holland, W. S., et al. 2012, in Society of Photo-Optical Instrumentation Engineers (SPIE) Conference Series, Vol. 8452, Millimeter, Submillimeter, and Far-Infrared Detectors and Instrumentation for Astronomy VI, ed. W. S. Holland & J. Zmuidzinas, 845208

Calvo, M., Benoît, A., Catalano, A., et al. 2016, Journal of Low Temperature Physics, 184, 816

Chapin, E. L., Berry, D. S., Gibb, A. G., et al. 2013, MNRAS, 430, 2545

Cookson, J. L., Bintley, D., Li, S., et al. 2018, in Society of Photo-Optical Instrumentation Engineers (SPIE) Conference Series, Vol. 10708, Proceedings of SPIE, 1070839

Coulson, I. M., Liu, F.-C., Cordiner, M. A., et al. 2020, AJ, 160, 182

Currie, M. J., Berry, D. S., Jenness, T., et al. 2014, in Astronomical Society of the Pacific Conference Series, Vol. 485, Astronomical Data Analysis Software and Systems XXIII, ed. N. Manset & P. Forshay, 391

Dempsey, J. T., & Friberg, P. 2008, in Ground-based and Airborne Telescopes II, ed. L. M. Stepp & R. Gilmozzi, Vol. 7012, International Society for Optics and Photonics (SPIE), 1472 – 1482. <https://doi.org/10.1117/12.787471>

Dempsey, J. T., Holland, W. S., Chrysostomou, A., et al. 2012, in Society of Photo-Optical Instrumentation Engineers (SPIE) Conference Series, Vol. 8452, Millimeter, Submillimeter, and Far-Infrared Detectors and Instrumentation for Astronomy VI, ed. W. S. Holland & J. Zmuidzinas, 845202

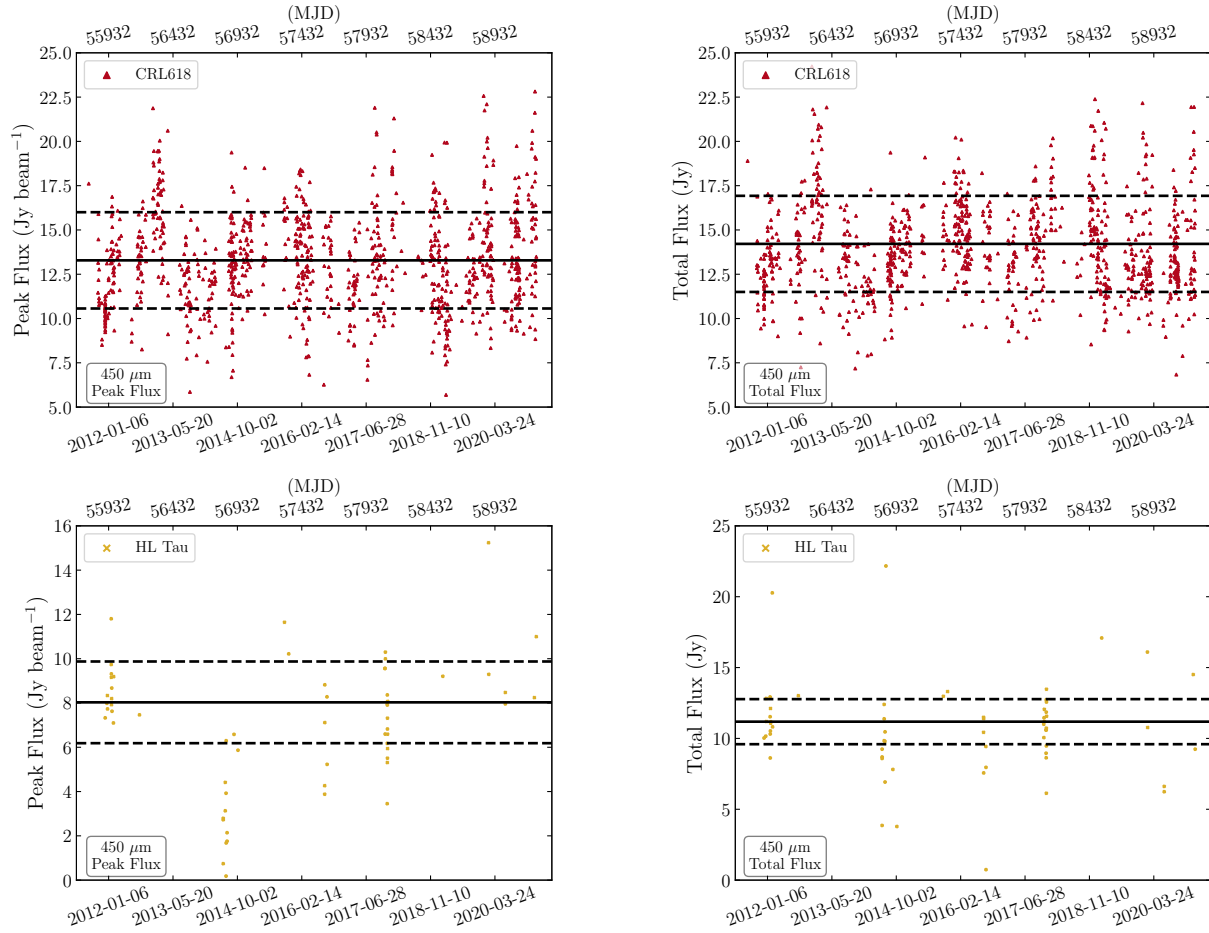


Figure 14. The peak (*left*) and total (*right*) fluxes derived for secondary-calibrator sources CRL 618 (*top*) and HL TAU (*bottom*) at $450\ \mu\text{m}$ using the FCFs presented in Table 4, along with the modifications presented in Table 5. The solid line represents the median value of the distribution and the dashed line shows the standard deviation of the light curve.

Dempsey, J. T., Friberg, P., Jenness, T., et al. 2013, *MNRAS*, 430, 2534

Dharmawardena, T. E., Kemper, F., Srinivasan, S., et al. 2019, *MNRAS*, 489, 3218

Dicker, S., Mason, B. S., Korngut, P. M., et al. 2009, in *American Astronomical Society Meeting Abstracts*, Vol. 213, American Astronomical Society Meeting Abstracts #213, 474.27

Dicker, S. R., Ade, P. A. R., Aguirre, J., et al. 2014, in *Society of Photo-Optical Instrumentation Engineers (SPIE) Conference Series*, Vol. 9153, Millimeter, Submillimeter, and Far-Infrared Detectors and Instrumentation for Astronomy VII, ed. W. S. Holland & J. Zmuidzinas, 91530J

Dowell, C. D., Allen, C. A., Babu, R. S., et al. 2003, in *Society of Photo-Optical Instrumentation Engineers (SPIE) Conference Series*, Vol. 4855, Millimeter and Submillimeter Detectors for Astronomy, ed. T. G. Phillips & J. Zmuidzinas, 73–87

Dunne, L., Eales, S., Edmunds, M., et al. 2000, *MNRAS*, 315, 115

Friberg, P., Berry, D., Savini, G., et al. 2018, in *Society of Photo-Optical Instrumentation Engineers (SPIE) Conference Series*, Vol. 10708, Millimeter, Submillimeter, and Far-Infrared Detectors and Instrumentation for Astronomy IX, ed. J. Zmuidzinas & J.-R. Gao, 107083M

Geach, J. E., Chapin, E. L., Coppin, K. E. K., et al. 2013, *MNRAS*, 432, 53

Ginsburg, A., Anderson, L. D., Dicker, S., et al. 2020, *ApJS*, 248, 24

Herczeg, G. J., Johnstone, D., Mairs, S., et al. 2017, *ApJ*, 849, 43

Holland, W. S., Robson, E. I., Gear, W. K., et al. 1999, *MNRAS*, 303, 659

Holland, W. S., Bintley, D., Chapin, E. L., et al. 2013, *MNRAS*, 430, 2513

Hughes, A. M., Wilner, D. J., Mason, B., et al. 2012, *ApJ*, 750, 82

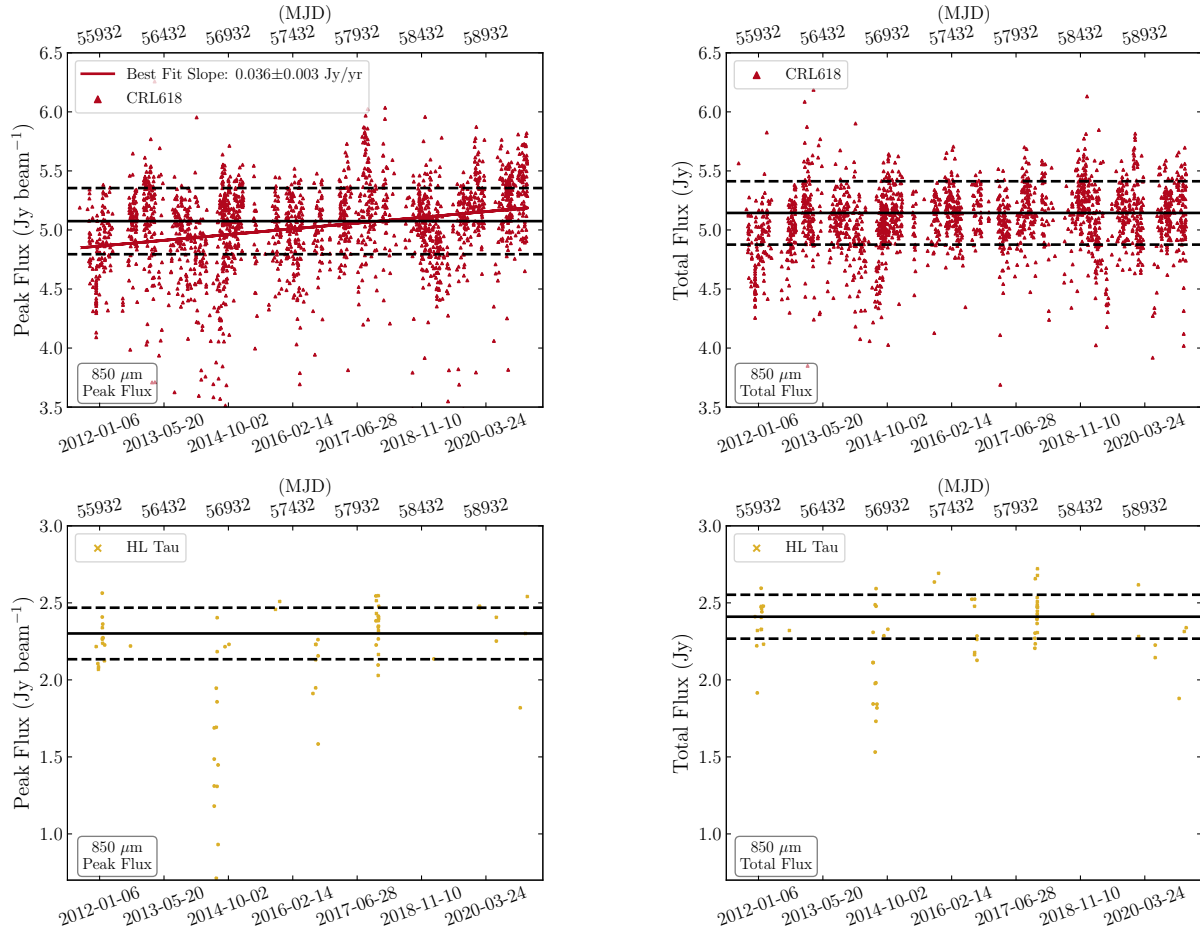


Figure 15. The peak (*left*) and total (*right*) fluxes derived for secondary-calibrator sources CRL 618 (*top*) and HL TAU (*bottom*) at $850\ \mu\text{m}$ using the FCFs presented in Table 4, along with the modifications presented in Table 5. The solid line represents the median value of the distribution and the dashed line shows the standard deviation of the light curve.

Hunter, J. D. 2007, *Computing In Science & Engineering*, 9, 90

Jenness, T., Chapin, E. L., Berry, D. S., et al. 2013, SMURF: Submillimeter User Reduction Facility, Astrophysics Source Code Library., ASCL, ascl:1310.007:

Jenness, T., Robson, E. I., & Stevens, J. A. 2010, *MNRAS*, 401, 1240

Jenness, T., Stevens, J. A., Archibald, E. N., et al. 2002, *MNRAS*, 336, 14

Klaas, U., Haas, M., Müller, S. A. H., et al. 2001, *A&A*, 379, 823

Knapp, G. R., Sandell, G., & Robson, E. I. 1993, *ApJS*, 88, 173

Kreysa, E., Bertoldi, F., Gemuend, H.-P., et al. 2003, in *Society of Photo-Optical Instrumentation Engineers (SPIE) Conference Series*, Vol. 4855, *Millimeter and Submillimeter Detectors for Astronomy*, ed. T. G. Phillips & J. Zmuidzinas, 41–48

Landolt, A. U. 1968, *ApJ*, 153, 151

Li, Z., Li, Z., Smith, M. W. L., et al. 2020, *MNRAS*, 492, 195

Lisenfeld, U., Isaak, K. G., & Hills, R. 2000, *MNRAS*, 312, 433

Liu, T., Kim, K.-T., Juvela, M., et al. 2018, *ApJS*, 234, 28

Lourie, N. P., Ade, P. A. R., Angile, F. E., et al. 2018, in *Society of Photo-Optical Instrumentation Engineers (SPIE) Conference Series*, Vol. 10708, *Millimeter, Submillimeter, and Far-Infrared Detectors and Instrumentation for Astronomy IX*, ed. J. Zmuidzinas & J.-R. Gao, 107080L

Lunde, E., Ade, P., Berthoud, M., et al. 2020, in *Society of Photo-Optical Instrumentation Engineers (SPIE) Conference Series*, Vol. 11453, *Society of Photo-Optical Instrumentation Engineers (SPIE) Conference Series*, 114534A

Mairs, S., Bell, G. S., Johnstone, D., et al. 2018, *The Astronomer’s Telegram*, 11583, 1

Mairs, S., Lalchand, B., Bower, G. C., et al. 2019, *ApJ*, 871, 72

Table 8. Secondary-calibrator Flux Information

Source	MJD	τ_{225}^a	A^b	450 μm Peak ^c (Jy beam ⁻¹)	450 μm Total ^d (Jy)	850 μm Peak ^c (Jy beam ⁻¹)	850 μm Total ^d (Jy)
...
Arp220	56997.8166	0.064	1.053	5.53	6.55	0.87	0.83
Arp220	56998.7641	0.057	1.216	5.88	5.68	0.84	0.77
Arp220	56999.7709	0.057	1.173	5.98	6.35	0.86	0.85
Arp220	57000.7346	0.060	1.360	7.06	6.90	0.93	0.81
Arp220	57000.7840	0.058	1.116	6.35	7.40	0.89	0.87
Arp220	57001.7033	0.049	1.625	7.19	8.26	0.93	0.96
Arp220	57001.7754	0.049	1.135	7.16	6.84	0.95	0.89
Arp220	57001.8224	0.053	1.025	6.11	6.99	0.99	0.80
Arp220	57002.8384	0.051	1.008	4.79	6.74	0.91	1.66
Arp220	57002.7228	0.045	1.408	6.88	8.28	0.88	0.93
...

NOTE—^aThe opacity of the atmosphere at 225 GHz at the time of the observation.

^bThe airmass at the time of the observation.

^cPeak fluxes were measured by performing a Gaussian fit to the source while the data was still in units of picowatts, then applying the FCFs and FCF corrections in Tables 4 and 5.

^dTotal fluxes were measured using aperture photometry while the data was still in units of picowatts. The total flux was calculated within a 1 arcminute diameter aperture centered on the source. The background level was determined using an annulus with inner diameter 1.5 arcminutes and outer diameter 2 arcminutes. The FCFs and FCF corrections in Tables 4 and 5 were applied.

- Marsh, K. A., Dowell, C. D., Velusamy, T., Grogan, K., & Beichman, C. A. 2006, *The Astrophysical Journal Letters*, 646, L77
- Neugebauer, G., Habing, H. J., van Duinen, R., et al. 1984, *ApJL*, 278, L1
- Ney, E. P., Merrill, K. M., Becklin, E. E., Neugebauer, G., & Wynn-Williams, C. G. 1975, *ApJL*, 198, L129
- Orton, G. S., Moses, J. I., Fletcher, L. N., et al. 2014, *Icarus*, 243, 471
- Parsons, H., Dempsey, J., Bintley, D., et al. 2020, in *Society of Photo-Optical Instrumentation Engineers (SPIE) Conference Series*, Vol. 11449, Society of Photo-Optical Instrumentation Engineers (SPIE) Conference Series, 114490I
- Perotto, L., Ponthieu, N., Macías-Pérez, J. F., et al. 2020, *A&A*, 637, A71
- Rigopoulou, D., Lawrence, A., & Rowan-Robinson, M. 1996, *MNRAS*, 278, 1049
- Robitaille, T., & Bressert, E. 2012, *APLpy: Astronomical Plotting Library in Python*, *Astrophysics Source Code Library*, ASCL, ascl:1208.017
- Saintonge, A., Wilson, C. D., Xiao, T., et al. 2018, *MNRAS*, 481, 3497
- Sakamoto, K., Wang, J., Wiedner, M. C., et al. 2008, *ApJ*, 684, 957
- Sandell, G. 2003, in *ESA Special Publication*, Vol. 481, *The Calibration Legacy of the ISO Mission*, ed. L. Metcalfe, A. Salama, S. B. Peschke, & M. F. Kessler, 439
- Schuller, F., Menten, K. M., Contreras, Y., et al. 2009, *A&A*, 504, 415
- Seiffert, M., Borys, C., Scott, D., & Halpern, M. 2007, *MNRAS*, 374, 409
- Shim, H., Kim, Y., Lee, D., et al. 2020, *MNRAS*, 498, 5065
- Simpson, J. M., Smail, I., Swinbank, A. M., et al. 2019, *ApJ*, 880, 43
- Siringo, G., Kreysa, E., Kovács, A., et al. 2009, *A&A*, 497, 945
- Smith, I. A., Tanvir, N. R., & Perley, D. A. 2018, *The Astronomer's Telegram*, 11781, 1
- Soifer, B. T., Helou, G., Lonsdale, C. J., et al. 1984, *ApJL*, 283, L1
- Stutzki, J., & Guesten, R. 1990, *ApJ*, 356, 513
- Tetarenko, A. J., Sivakoff, G. R., Miller-Jones, J. C. A., et al. 2017, *MNRAS*, 469, 3141
- Truch, M. D. P., Ade, P. A. R., Bock, J. J., et al. 2008, *ApJ*, 681, 415

- Wang, W.-H., Lin, W.-C., Lim, C.-F., et al. 2017, ApJ, 850, 37
- Ward-Thompson, D., Di Francesco, J., Hatchell, J., et al. 2007, PASP, 119, 855
- Ward-Thompson, D., Pattle, K., Bastien, P., et al. 2017, ApJ, 842, 66
- Westbrook, W. E., Becklin, E. E., Merrill, K. M., et al. 1975, ApJ, 202, 407
- Wiedner, M. 1998, PhD thesis, University of Cambridge
- Wilson, C. D., Warren, B. E., Israel, F. P., et al. 2009, ApJ, 693, 1736